國立臺灣大學理學院物理學系

碩士論文

Graduate Institute of Physics

College of Science

National Taiwan University

Master Thesis

光/電/磁可控雙閘式雙極有機光電晶體

An optical/electrical/magnetic controllable

dual-gate phototransistor

蔡佳霖

Chia-Lin Tsai

指導教授：陳永芳　博士

許芳琪　博士

Advisor: Yang-Fang Chen, Ph.D.

Fang-Chi Hsu, Ph.D.

中華民國 110 年 7 月

July, 2021

國立臺灣大學碩士學位論文
口試委員會審定書
光/電/磁可控雙閘式雙極有機光電晶體
An optical/electrical/magnetic controllable
dual-gate phototransistor

本論文係蔡佳霖君（R08222062）在國立臺灣大學物理學所完成之碩士學位論文，於民國 110 年 7 月 26 日承下列考試委員審查通過及口試及格，特此證明

口試委員：

_____ （簽名）
（指導教授）

_____　_____

_____　_____

_____　_____

I

誌謝

感謝陳永芳老師及許芳琪老師兩位指導教授兩年來的指導，在每次的 meeting 給予我許多的建議並且提供了許多方向及方法讓我能順利完成這個題目。也感謝夏玉學姊及家宇學長，在實驗過程遇到困難或者是需要架設量測系統的時候給予我許多的幫助及意見。當然還有承勳學長將各個元件的製程仔細地教給我讓我能夠順利的完成這個題目。當然還有 R415 的各位同學，除了彼此討論互相幫忙解決實驗上遇到的問題之外，偶爾也可以閒聊講一些垃圾話陪我度過很多因為實驗進度無法推進而感到痛苦的時光。感謝我的家人讓我能夠無後顧之憂地唸完兩年的研究所。最後感謝這兩年間出現在我生活中的所有人，不管是認識超過 10 年的國中同學們，還是研究所期間新認識的朋友，讓我的生活不只有實驗跟念書，偶爾可以出門走走，偶爾可以去玩桌遊，偶爾可以做各種不同的事情轉換心情，讓我的研究所生活過得更豐富。

中文摘要

我們在此提出一種可透過光/電/磁三種變因控制的雙閘式雙極有機光電晶體。此光電晶體以垂直方式整合有機太陽能電池(ITO/ZnO/P3HT:P C_{61} BM/Mo O_3 /Ag)、電阻式隨機存取記憶體(Ag/PMMA/Au)及具金字塔結構的磁電元件(FeNi/PDMS/AgNWs)。此元件具有上述三種元件分別的特性,透過對於光、電場、磁場的反應形成雙閘式光電晶體。和傳統的光電晶體相比,此元件具有超快的光響應時間、可調節的光電流、高開關電流比率及非接觸式人機互動等特性,這些獨特的特性均有利於高速光通訊及電路微型化。此外,這種光電晶體具有獨特的數位邏輯特性,使其在光通訊及資訊安全領域的應用具有莫大的潛力。


關鍵字:超快光響應、光通訊、有機太陽能電池、電阻式隨機存取記憶體、光電晶體、磁電元件、非接觸式元件

ABSTRACT

Higher data transmission rates, broader bandwidths, better privacy and security are indispensable for the current information-explosive age. However, to achieve the desired functionality still remains as a great challenge. In this study, an optical/electrical/magnetic dual-gate phototransistor is proposed, fabricated and demonstrated, which can be controlled by light, electric and magnetic field. This phototransistor uses a tandem structure composed of an organic solar cell (OSC) of ITO/ZnO/P3HT:PC_{61}BM/MoO_3/Ag, a resistive random access memory (RRAM) of Ag/PMMA/Au and a magnetoelectronic film with micropyramid structure of FeNi/PDMS/AgNWs. This device processes the properties of each individual component enabling to response to light, electric and magnetic fields and work as a dual-gate transistor. Compared with conventional transistor, our proposed device carries several intriguing features, such as ultra-fast response time, controllable photocurrent with a variety of external stimuli, high ON/OFF ratio, and touchless human-machine interaction. All of above features are beneficial for high speed optical communication and circuit miniaturization. Furthermore, its unique logical characteristics have great potential to be implemented into

information security for the future development of Li-Fi optical communication.
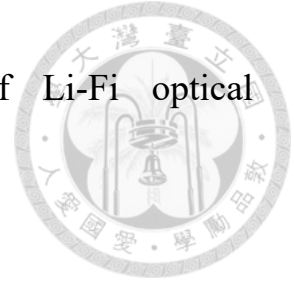
Keyword: ultra-fast response, Li-Fi optical communication, information encryption, dual-gate phototransistor, magnetoelectronic device, touchless

Content

List of Figure and Tables

Chapter 1　Introduction

　　Nowadays, we live in an age of information explosion because of the rapid improvement of the technologies. People have demands for faster calculation, faster transmission and wireless communication technology to access information instantly. Li-Fi, one of the major technologies of the optical communication, is highly expected to be a popular communication system and wireless internet access in the future. Because of the increasing demand of the data transmission, traditional RF communication suffers many problems such as bandwidth limit and security issues. To overcome these problems, light-fidelity (Li-Fi) is one of the major technologies to be developed[1-3]. In general, Li-Fi technology uses visible light to offer several advantages such as higher data transmission rates, broader bandwidths, better privacy and security, and less expensive equipment, which cannot be achieved based on traditional Wi-Fi technology[4-7]. Photodetectors including photodiode and phototransistor can sense the light signal effectively. Different from photodiode, phototransistor can not only sense light signals but also have switchable state of conducting state and insulating state controlled by the third electrode called gate[8,9]. This switchable property enables phototransistor can not only be a photodetector but also be a logic

1
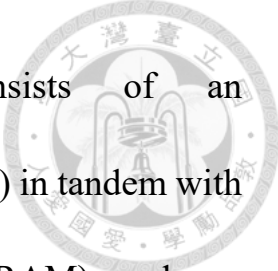
device, making it have more potential application than photodiode in information technology.
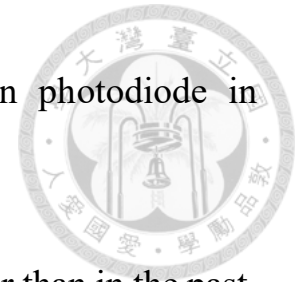
Recently, the size of the electronics are becoming smaller than in the past. Inevitably, they are desired to be wearable and touchless. Flexible and touchless electronics is believed to be indispensable in the future electronic devices[10-13]. Touchless characteristics are usually achieved by using interaction with physical fields such as magnetic field, electric field, and etc. For example, the Hall effect and giant magneto-resistance (GMR) are commonly used in the currently reported magnetic sensors[14-19]. By endowing electronic device with magnetic sensing capability, flexible electronics can upgrade to be touchless and diverse their applications in a variety of wearable smart systems, including human-machine interactivity, medical care, soft robot, and etc.[20-23]

Organic phototransistor, an indispensable role in optoelectronics, is a sensitive transistor with switchable photocurrent controlled by the third electrode gate. Recently, it has been revealed that the output current of the phototransistor can be modulated by electric field[24], magnetic field[25], light[26,27], and etc. In this study, we propose an optical/electrical/magnetic double-gate phototransistor, which can be controlled by light, electric and

magnetic field. This novel phototransistor consists of an ITO/ZnO/P3HT:PC$_{61}$BM/MoO$_3$/Ag organic solar cell (OSC) in tandem with a Ag/PMMA/Au resistive random access memory (RRAM) under a FeNi/PDMS/AgNWs magnetoelectronic film 80 μm away defined by a PET film. The FeNi/PDMS/AgNWs structure uses the Au layer of the bottom RRAM to serve as its second electrode and form a magnetoelectronic device. The output current of the phototransistor can be controlled by the status of RRAM and magnetoelectronic device, working as a gate electrode in conventional dual-gate transistor. Compared with conventional phototransistor, our device possesses several advantages, such as high ON/OFF ratio, ultra-fast photoresponse time, touchless interaction, and controllable photocurrent with a variety of external stimuli. Notably, optical, electrical, and magnetic modulation features of the proposed phototransistor diversify its applications in information technology for Li-Fi communications and information encryption, which should be very useful and timely for the emerging explosive social media.

Reference

1. L. U. Khan, Visible light communication: Applications, architecture, standardization and research challenges, Digital Commun. Networks 3, 78–88 (2017).

2. J. Shi, J. He, R. Deng, Y. Wei, F. Long, Y. Cheng, and L. Chen, Multilevel modulation scheme using the overlapping of two light sources for visible light communication with mobile phone camera, Opt. Express 25,15905–15912 (2017).

3. M. Bock, P. Eich, S. Kucera, M. Kreis, A. Lenhard, C. Becher, and J. Eschner, High-fidelity entanglement between a trapped ion and a telecom photon via quantum frequency conversion, Nat. Commun. 9, 1998 (2018).

4. W.-Y. Lin, C.-Y. Chen, H.-H. Lu, C.-H. Chang, Y.-P. Lin, H.-C. Lin, and H.-W. Wu, 10m/500Mbps WDM visible light communication systems, Opt. Express 20, 9919–9924 (2012).

5. L. Grobe, A. Paraskevopoulos, J. Hilt, D. Schulz, F. Lassak, F. Hartlieb, C.Kottke, V. Jungnickel, and K.-D. Langer, High-Speed Visible Light Communication Systems, IEEE Commun. Mag. 51, 60–66(2013).

6. A. Kumar, A. Mihovska, S. Kyriazakos, and R. Prasad, Visible Light Communications (VLC) for Ambient Assisted Living Wireless, Pers. Commun. 78, 1699–1717 (2014).

7. S. Rajbhandari, H. Chun, G. Faulkner, K. Cameron, A. V. Jalajakumari, R.Henderson, D. Tsonev, M. Ijaz, Z. Chen, and H. Haas, High-Speed Integrated Visible Light Communication System: Device Constraints and Design Considerations, IEEE J. Sel. Areas Commun. 33, 1750–1757 (2015).

8. K. J. Baeg, M. Binda, D. Natali, M. Caironi, and Y. Y. Noh, Organic Light Detectors: Photodiodes and Phototransistors, Adv. Mater. 25, 4267–4295 (2013).

9. P. Gu, Y. Yao, L. Feng, S. Niu, and H. Dong, Recent advances in polymer phototransistors, Polym. Chem. 6, 7933–7944 (2015).

10. D.H. Kim, N. Lu, R. Ma, Y.S. Kim, R.H. Kim, S. Wang, J. Wu, S.M. Won, H. Tao, A. Islam, K.J. Yu, T.I. Kim, R. Chowdhury, Sensitive flexible magnetic sensors using organic transistors with magnetic-functionalized suspended gate electrodes, Adv. Mater. 27 7979–7985 (2015).

11. D.H. Kim, N. Lu, R. Ma, Y.S. Kim, R.H. Kim, S. Wang, J. Wu, S.M.
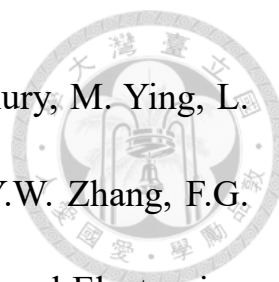
Won, H. Tao, A. Islam, K.J. Yu, T.I. Kim, R. Chowdhury, M. Ying, L. Xu, H.J. Chung, H. Keum, M. McCormick, P. Liu, Y.W. Zhang, F.G. Omenetto, Y. Huang, T. Coleman, J. A. Rogers, Epidermal Electronics, Science 333 838–843 (2011).

12. T. Sekitani, T. Yokota, U. Zschieschang, H. Klauk, S. Bauer, K. Takeuchi, M. Takamiya, T. Sakurai, T. Someya, Organic nonvolatile memory transistors for flexible sensor arrays, Science 326 1516–1519 (2009).

13. W. Wu, X. Wen, Z. Wang, Taxel-addressable matrix of vertical-nanowire piezotronic transistors for active and adaptive tactile imaging, Science 340 952–957 (2013).

14. M. Johnson, B. R. Bennett, M. J. Yang, M. M. Miller, B. V. Shanabrook, Hybrid Hall effect device, Appl. Phys. Lett. 71 974–976 (1997).

15. S. Thiele, R. Vincent, M. Holzmann, S. Klyatskaya, M. Ruben, F. Balestro, and W. Wernsdorfer, Electrical readout of individual nuclear spin trajectories in a single-molecule magnet spin transistor, Phys. Rev. Lett. 111 037203 (2013).

16. L. Bogani, W. Wernsdorfer, Molecular spintronics using single-molecule magnets, Nat. Mater. 7 179–186 (2008).

17. R. Jansen, The spin-valve transistor: a review and outlook, J. Phys. D:

Appl. Phys. 36 289–308 (2003).

18. M. M. Miller, P. E. Sheehan, R. L. Edelstein, C. R. Tamanaha, L. Zhong, S. Bounnak, L.J. Whitman, R.J. Colton, A DNA array sensor utilizing magnetic microbeads and magnetoelectronic detection, J. Magn. Magn. Mater. 225 138–144 (2001).

19. T. Dogaru, S. T. Smith, Giant magnetoresistance-based Eddy-current sensor, IEEE Trans. Magn. 37 3831–3838 (2001).

20. C.Y . Tzou, S. Y. Cai, C. Y. Tseng, C. Y. Chang, S. Y. Chiang, C. Y. Jiang, Y. H. Li, J. M. Ma, Y. M. Liao, F. C. Hsu, Y. F. Chen, An ultra-fast two-terminal organic phototransistor with vertical topology for information technologies. Appl. Phys. Lett., 114(19) 193301 (2019).

21. S. Y. Cai, C. H. Chang, H. I. Lin, Y. F. Huang, W. J. Lin, S. Y. Lin, Y. R. Liou, T. L. Shen, Y. H. Huang, P. W. Tsao, C. Y. Tzou, Y. M. Liao, and Y. F. Chen, Ultrahigh sensitive and flexible magnetoelectronics with magnetic nanocomposites: Toward an additional perception of artificial intelligence. ACS Appl. Mater. Interfaces, 10(20) 17393-17400 (2018).

22. C. Y. Jiang, C. H. Tsai, C. Y. Tzou, F. C. Hsu, and Y. F. Chen. Magnetically controllable and flexible phototransistors for artificial intelligent skin with additional perception. Organic Electronics 85

105849 (2020).

23. Meng Li, Yu Wang, Aiping Chen, Arin Naidu, Bradley S. Napier, Wenyi Li, C. L. Rodriguezb, S. A. Crookerd, and F. G. Omenetto, Flexible magnetic composites for light-controlled actuation and interfaces. PNAS, 115 8119-8124 (2018).

24. A. Péerez − Tomás, A. Lima, Q. Billon, I. Shirley, G. Catalan, and M. Lira−Cantú, A solar transistor and photoferroelectric memory, Adv. Funct. Mater. 28, 1707099 (2018).

25. M. N. Baibich, J. M. Broto, A. Fert, F. N. Van Dau, F. Petroff, P. Etienne, G. Creuzet, A. Friederich, and J. Chazelas, Giant magnetoresistance of (001)Fe/(001)Cr magnetic superlattices, Phys. Rev. Lett. 61, 2472 (1988).

26. I. Vlassiouk, C.-D. Park, S. A. Vail, D. Gust, and S. Smirnov, Control of nanopore wetting by a photochromic spiropyran: A light-controlled valve and electrical switch, Nano Lett. 6,1013–1017 (2006).

27. H. Ling, K. Tan, Q. Fang, X. Xu, H. Chen, W. Li, Y. Liu, L. Wang, M. Yi, and R. Huang, Light-tunable nonvolatile memory characteristics in photochromic RRAM, Adv. Electron. Mater. 3, 1600416 (2017).

Chapter 2 Theoretical Background

2.1 Solar spectrum

Because of the scattering and absorption of the atmosphere, solar radiation has longer length during propagation which makes the light intensity decays. To characterize the solar spectrum after traveling through the atmosphere, the air mass coefficient *(AM)* is defined by

$$AM = \frac{L}{L_0} \approx \frac{1}{\cos z} \qquad (2.1)$$

where L is the optical length that the radiation passes through the atmosphere, L_0 is the zenith path length or the atmosphere height, and z is zenith angle. The air mass coefficient (*AM*) is often referred to using the syntax "AM" following by a number. **Figure 2.1a** shows some special cases:

AM 0. The spectrum outside the atmosphere, which means "no atmosphere".

AM 1. The spectrum after traveling through the atmosphere to sea level with sun directly overhead. This means "one atmosphere".

AM 1.5. 1.5 atmosphere thickness, corresponding to a solar zenith angle of $z = 48.2°$.

Because the solar zenith angle depends on the time in a day, seasons and the latitude, solar cells do not generally operate under exactly AM 1. Thus, AM

9

1.5 is used to represent the overall year average for mid-latitude and to be a standard air mass condition for testing solar cells in the solar industries. However, solar spectrum is also affected by the moment, position, and even weather. American Society for Testing and Material (ASTM) defined an standard spectrum in the specified atmospheric conditions to compare solar modules. **Figure 2.1b** shows the solar spectral irradiance compared to two primary constituents: direct and diffuse radiation, so AM 1.5 is delineated into AM 1.5D and AM 1.5G, where "D" represents direct radiation and "G" means global irradiance including sky diffusion and radiation reflected by ground. The total light intensity equals to the integration of the spectra irradiance:

$$I_{light} = \int F(\lambda)\, d\lambda \qquad (2.2)$$

where I_{light} is the light intensity and $F(\lambda)$ is the solar spectral irradiance. The light intensity of AM 1.5G is $1000\ \text{W/m}^2$ which is the most common spectrum for measurements.[1]
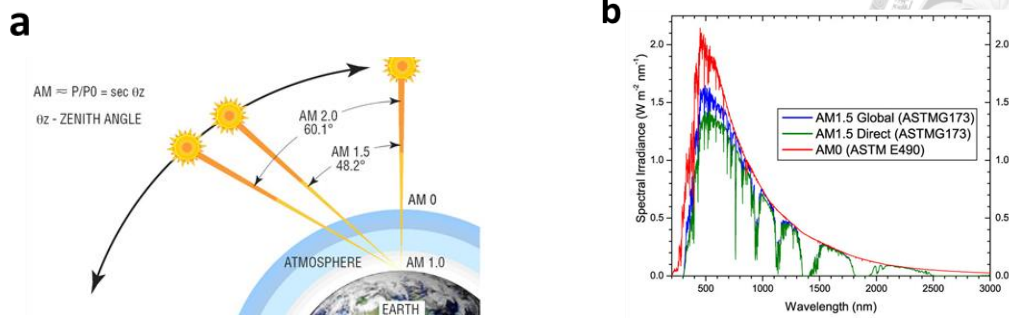
Figure 2.1 (a) The air mass in different zenith angle.[2] **(b)** Spectrums in

different air mass condition[3]

2.2 Models of solar cells

2.2.1 ideal model

Without illumination, solar cell consists of a p-n junction structure and the

current is caused by the injection and diffusion of carriers at the

donor/acceptor interface. Thus, the current density to voltage behavior can

be described by equation of diode:

$$J_D = J_0 \left[\exp\left(\frac{qV}{k_BT}\right) - 1\right] \tag{2.3}$$

where J_0 is reverse-saturation current density, q is the charge of electron,

k_B is Boltzman constant, T is absolute temperature (K). The current J_D

which is measured under dark condition is called dark current.

With illumination, the excitons are generated as the photon absorption and

11
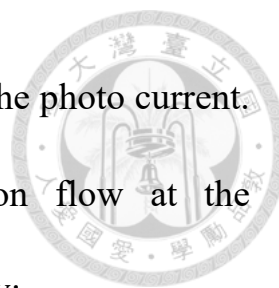
following separated by the build-in electric which lead to the photo current. These photo current flows oppositely to the injection flow at the donor/acceptor interface, so the total current is described by:

$$J = J_{ph} - J_D = J_{ph} - J_0 \left[\exp\left(\frac{qV}{k_BT}\right) - 1\right] \qquad (2.4)$$

where J_{ph} is the photo current. The current density shown in **Figure 2.2a** assumes that we treat the solar cell as a generator. **Figure 2.2b** shows the current density assuming the solar cell is tested as a load and the total current is expressed as:

$$J = J_0 \left[\exp\left(\frac{qV}{k_BT}\right) - 1\right] - J_{ph} \qquad (2.5)$$
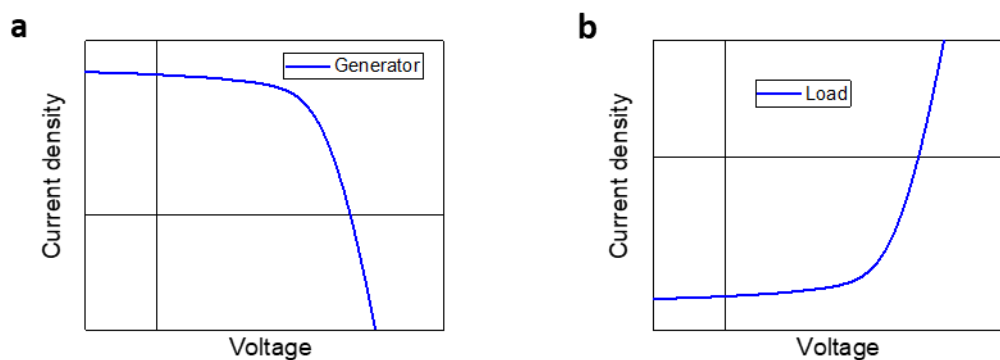
Figure 2.2 *J-V* characteristics of a solar cell treated as a **(a)** generator **(b)** load.

2.2.2 non-ideal model

● Ideality factor

The derivation of the simple diode equation uses the certain assumption about the cell. But actually there are second order effects so that the diode does not behave ideally. Thus, The ideality factor which is denoted by n is introduced to describe how closely the diode follows the ideal diode equation:

$$J = J_0 \left[\exp\left(\frac{qV}{nk_BT}\right) - 1\right] - J_{ph} \tag{2.6}$$

In ideal case, all recombination occurs via band to band or recombination via trap in the bulk areas from the device is assumed (i.e. not in the junction). Under this assumption, the ideality factor n is equal to one. However, recombination does occur in other ways and areas of the device in real condition which makes n deviate from one such as high level infection, Shockley-Read-Hall recombination, etc.
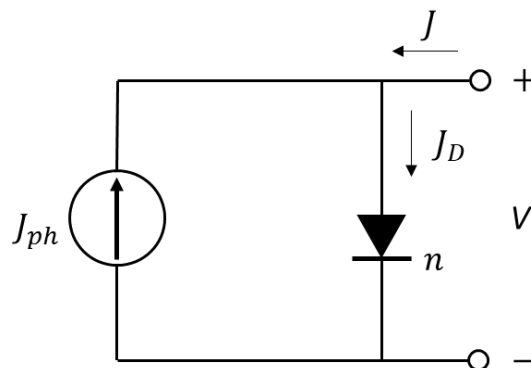
Figure 2.3 Equivalent circuit with ideality factor n.

● Resistive effect

Additionally, the resistive effect in solar cell needs to be considered which

dissipates power in the resistances can lead to reduce the efficiency of the

solar cell. As shown in **Figure 2.4**, there are two pares in the equivalent

circuit of considering resistive effect: series resistance R_s and shunt

resistance R_{sh}. The series resistance R_s is caused by bulk resistance,

electrode resistance and contact resistance. R_s maked voltage drop to the

output, so it should be as small as possible. The shunt resistance R_{sh} is

typically caused by manufacturing defects which provides an alternating

current path for the photocurrent making the output current loss. Thus, R_{sh}

should be large to make leakage current less. Considering the resistive effect,

the current density to voltage equation can be expressed as:

$$J = J_{ph} - J_0 \left\{ \exp\left[\left(\frac{q(V+JR_s)}{nk_BT}\right)\right] - 1 \right\} - \frac{(V+JR_s)}{R_{sh}} \qquad (2.7)$$
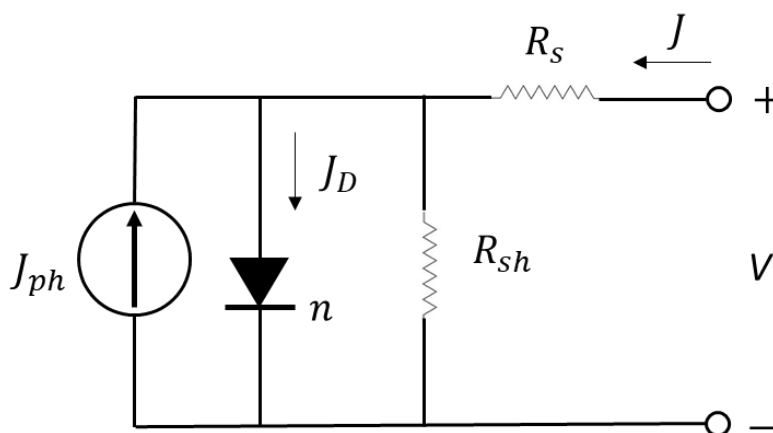
Figure 2.4 Equivalent circuit with considering resistive effect

14

2.3 Parameters of solar cells

2.3.1 Quantum efficiency (QE)

Quantum efficiency indicates the number of carriers produced by the solar cell when the irradiated by photons of particular wavelength. There are two types of quantum efficiency are often considered

External quantum efficiency (EQE) is the ratio of the of charge carriers collected by the electrode to the number of photons of the given wavelength illuminating on the solar cell from outside (incident photon)

$$EQE(\lambda) = \frac{carriers/sec}{phtons/sec} = \frac{currents/q}{incident\ power/(\frac{hc}{\lambda})} \qquad (2.8)$$

Internal quantum efficiency (IQE) is the ratio of the number of the charge carriers collected by the electrode to the number of photons of a given wavelength illuminating on the solar cell from outside and are absorbed by the cell.

$$IQE(\lambda) = \frac{carriers/sec}{absorbed\ phtons/sec} = \frac{EQE(\lambda)}{1-Reflection} \qquad (2.9)$$

where λ is wavelength, *h* is Planck constant and c is light speed in vacuum. External Quantum Efficiency is also called incident photon-to-electron conversion efficiency (IPCE).

15

2.3.2 Spectral response (*SR*)

Spectral response is similar to EQE. Spectral response is defined by the ratio of the photocurrent response to the incident power of a given wavelength illuminating on the solar cell from outside.

$$SR(\lambda) = \frac{current}{incicdent\ power} = \frac{q\lambda}{hc}EQE(\lambda) \qquad (2.10)$$

2.3.3 Short circuit current density (J_{sc})

The short circuit current density J_{sc} is the output current of the solar cell under short circuit condition which means the load resistance is zero, namely the applied voltage V is zero. It is the maximum current density that a solar cell can output. In the model of Equation (2.6) with this condition, we get:

$$J_{sc} = J_{ph} \qquad (2.11)$$

J_{sc} can not only be obtained by *J-V* measurement, but also by *EQE* measurement:

$$J_{sc} = \int SR(\lambda) \cdot F(\lambda)\, d\lambda = \int \frac{q\lambda}{hc}\, EQE(\lambda) \cdot F(\lambda)\, d\lambda \qquad (2.12)$$

Where $F(\lambda)$ is the spectral irradiance of the incident light. From Equation (2.12), $F(\lambda)$ is proportional to light intensity at given air mass condition, and *EQE* is normally independent on light intensity. Thus, J_{sc} is proportional to light intensity from Equation 2.11:

16

$$J_{sc} = J_{ph} \propto I_{light} \tag{2.13}$$

Where I_{light} is the intensity of the incident light

2.3.4 Open circuit voltage (V_{oc})

The open circuit voltage is the output voltage of the solar cell under open circuit condition which has infinite load resistance, that is to say, there is no current flow through the solar cell in this condition. It is the maximum voltage that solar cell can output. We can get V_{oc} from Equation (2.6) by setting current density zero:

$$V_{oc} = n\frac{k_B T}{q}\ln\left(\frac{J_{ph}}{J_0} + 1\right) \tag{2.14}$$

Equation (2.14) shows that V_{oc} is depends on the saturation current pf the solar cell and the light-generated current. As the carrier recombination affects the loss of light-generated current, gaining a discernment of the mechanisms governing the recombination is vital for enhancing the solar cell performance and V_{oc}. In V_{oc} to log scale light intensity curve, different slope or different intensity factor n, will be correspond to different recombination mechanisms.

2.3.5 Power convert efficiency (*PCE*, η) and Fill faceor (*FF*)

Power convert efficiency (*PCE*, η) is an important parameter to understand the performance of a solar cell. In the *J-V* characteristic curve of the solar cell, each point will be correspond to a rectangular area which means the output power per unit area of the solar cell. At point M_{pp} point in the J-V curve where the maximum power is generated with the current density J_m and the voltage V_m, then the *PEC* can be defined as the maximum power output from the solar cell to the incident power:

$$PCE = \frac{J_m V_m}{I_{light}} = \frac{J_{sc} V_{oc} FF}{I_{light}} \qquad (2.15)$$

where I_{light} is the intensity incident to the device, and *FF* is expressed by:

$$FF = \frac{J_m V_m}{J_{sc} V_{oc}} \qquad (2.16)$$

FF characterize how "square" the J-V curve is and it represents how "easy" or how "difficult" the photogenerated carriers can be extracted out of a photovoltaic device.

2.4 Organic solar cells (OSCs)

2.4.1 Organic semiconductor

The organic semiconductor is the conductive organic material that has semiconductor properties which can attribute to its conjugate chain. In **Figure 2.5,** conjugated chain consists of alternating single and double bonds along the backbone. The carbon atoms in conjugated chain are connected to each other by sp^2 hybridization forming a binding σ-molecular orbitals (MOs), and the electrons in σ-MOs are highly localized. In contrast, the remaining p_z-orbitals form the bonding π-MOs and the anti-bonding π*-MOs which are delocalized across the entire conjugate chain where electrons can move easily. The more p_z-orbitals combine, the more delocalized MOs are formed. At infinity, the bonding π-MOs and anti-bonding π*-MOs form continuous energy states rather than discrete energy levels. At ground state the bonding π-MOs are full of electrons and the anti-bonding π*-MOs are vacant. The highest state formed by bonding π-MOs is called Highest Occupied Molecular Orbital (HOMO) and the lowest state formed by anti-bonding π*-MOs is called Lowest Unoccupied Molecular Orbital (HOMO). The gap between the HOMO and LUMO is called bandgap.[4]

19
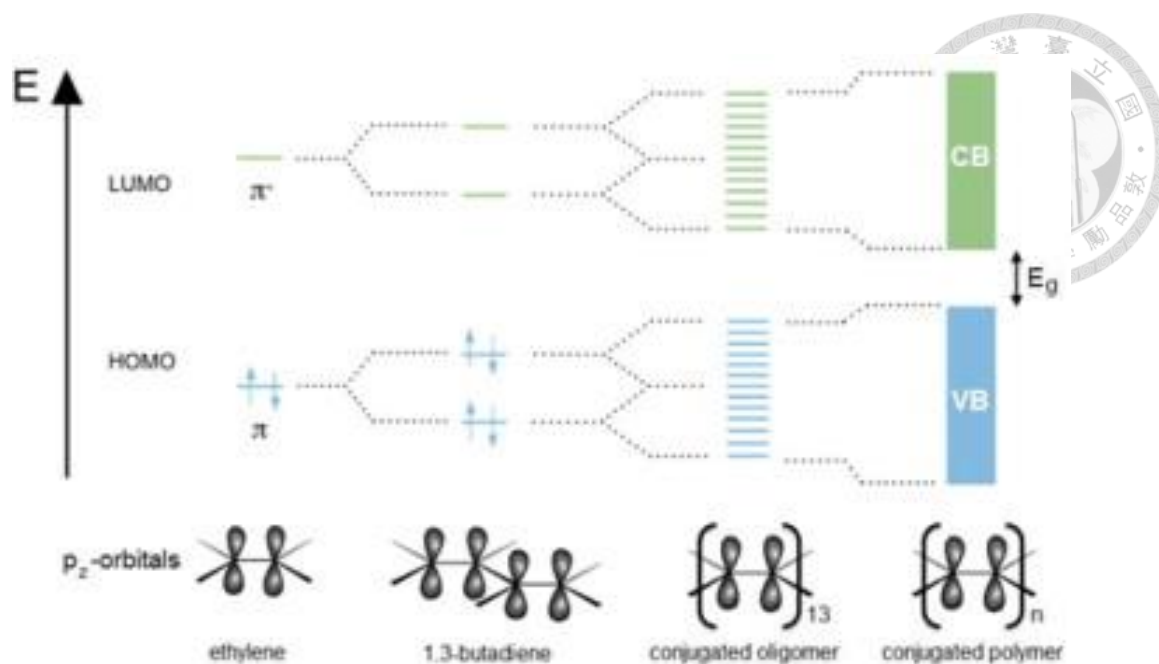
Figure 2.5 The evolution of the HOME and LUMO of a polymer[4]

Organic molecular stack each other by Van der Waals bonds forming solid state. Because of the interaction between the molecules, HOMO and LUMO levels in the solid state is different from that of the molecule. However, Van der Waals bond is a weak reaction, so HOME and LUMO will not change so much. HOMO and LUMO of the molecule are still valid in the solid. **Figure 2.6** shows the evolution of the energy levels of a molecular solid forming single-molecule levels.[5]
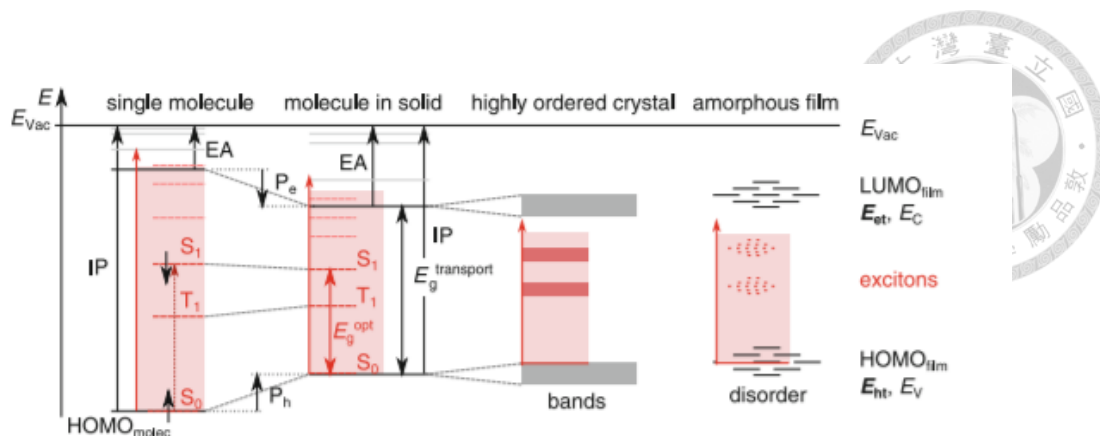
Figure 2.6 The evolution of the energy levels of a molecular solid from single-molecule levels.[5]

2.4.2 Structures of OSCs

Organic solar cells gave been developed for many years. there are manty different structures of OSCs, and we usually take p-i-n structure recently. This structure consist of an intrinsic between n-doped and p-doped wide-gap charge transport layers. The intrinsic structure, which is also called active layer, is an absorber layer contains donor and acceptor, polymers or small molecules are usually treated as the donor, and fullerene derivatives are treated as acceptor. There are some possible realizations of the intrinsic structure: flat/planar/bilayer heterojunction (FHJ, bilayer), bulk heterojunction (BHJ, blend). The exciton has to reach a D-A interface to spilt. However, the exciton diffusion distance is too short in most organic material

which causes some carriers recombine resulting the loss of photocurrent. The bulk heterojunction is the way to overcome this problem by mixing donor and acceptor materials.

The p/n layers between the electrode and the active layer are also called hole/electron transport layer, respectively. There are some functions of the hole electron transport layer materials:[6]

1. Adjusting the energetic barrier height between the active layer and electrodes.

2. Selecting and blocking carriers. Holes will be blocked and the electrons are allowed pass through the ETL and HTL is opposite.

3. Prohibiting chemical and physical reaction between active layer and electrode.

4. To act as a optical spacer.

The common materials of ETL are ZnO, TiO_2, Ca, LiF, PFN, etc, and the common materials of HTL are MoO_3, V_2O_5, PEDOT:PSS, etc.

Organic solar cells can be divided into conventional and invert structure. The electrode of OSCs will be metals or transparent conducting electrode such as Indium Tin Oxide (ITO) and Fluorine Tin Oxide (FTO). If transparent electrode is used as anode that the device is called conventional

OSC, if used as cathode that the device is call inverted OSC.

a			b		
Low work function metal			High work function metal		
Electron transport layer			Hole transport layer		
Active layer			Active layer		
Hole transport layer			Electron transport layer		
ITO (anode)			ITO (anode)		
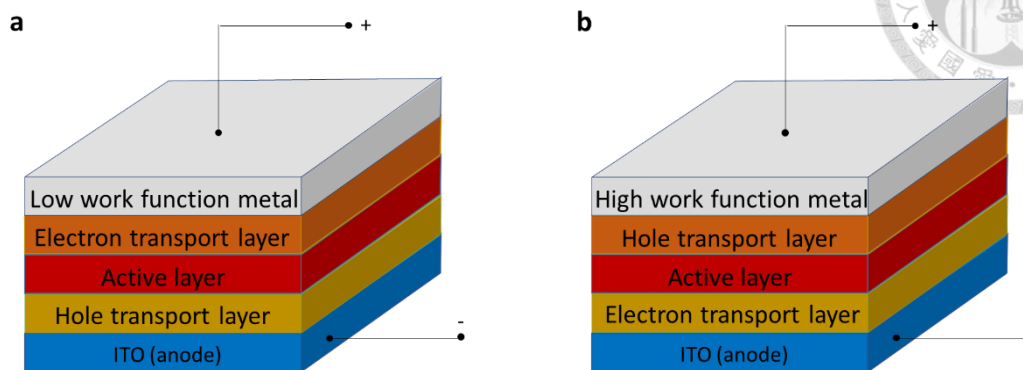
Figure 2.7 (a) Conventional and **(b)** invert device of organic solar cells

2.4.3 Photovoltaic effect

Photovoltaic effect is the primary principle which converts solar energy into electric energy. When a p-type semiconductor and n-type semiconductor contact to each other, the p-n junction will formed. Without illumination, an electric field is present internally in the junction region due to the carrier flow, it causes the additional electrons and holes are concentrated on the junction of p-type and n-type semiconductor, respectively. After light irradiating on the solar cell, photon are absorbed. If the energy of the absorbed photon is high enough , free electron-hole pairs will be produced, and the electron-hole pairs will be separated by the electric field moving electrons into n-type region and holes into p-type region generating

photocurrent. We can use four steps to illustrate the process for transferring radiation energy to electric energy:

1. Photons absorption and electron-hole pairs generated.

2. Diffusion of electrons and holes and carriers generation at donor/acceptor interface.

3. Charge carriers transport toward electrodes.

4. Electrons and holes are collected in opposite electrode.

2.5 Resistive random access memory (RRAM)

RRAM is a kind of non-volatile bitable memory and generally composed of a mersister sandwiched by two electrodes forming a capacitor-like metal-insulator-metal (MIM) architecture[7,8]. The interlayer can be organic, inorganic or metal-oxide. After an initial forming cycle, these MIM cells can be electrically switched between at least two different resistance state. By applying appropriate programming or write voltage pulse V_{wr}, cell in high-resistance state (HRS, or OFF state) can be set to a low-resistance state (LRS, or ON state).

24
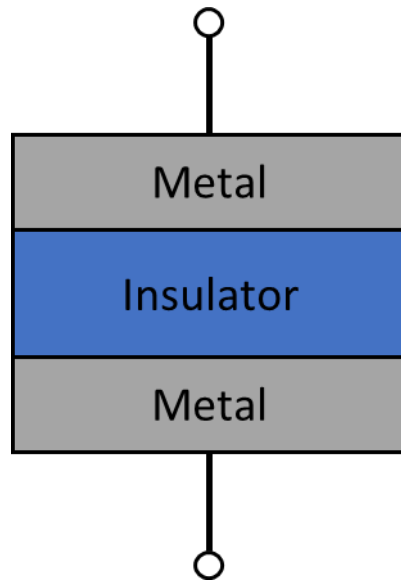
Figure 2.8 MIM structure.

2.5.1 Resistive switching behaviors

There are two different types of switching process with respect to the electrical polarity required for resistively switching cells (**Figure 2.9**). the switching process does not depend on the polarity of the writing voltage signal (**Figure 2.9a**) which called unipolar. During the set process, the current is typically limited by the compliance current of the controller. The RESET process occurs at a higher current and a voltage below the SET voltage. The SET process occurs at one voltage polarity and the RESET at the reversed voltage polarity (**Figure 2.9b**) which is called bipolar. To show bipolar switching behavior, the MIM system needs to have some asymmetry

such as different electrode material "M" or a dedicated voltage polarity during the initial forming step. Systems which can be changed by operation conditions between unipolar and bipolar operation have been nonpolar.
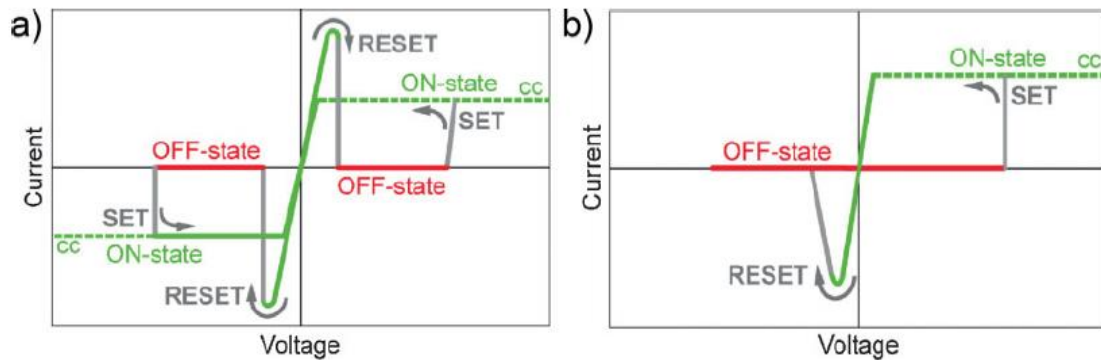
Figure 2.9 Resistive switching behaviors of a RRAM. **(a)** A unipolar RRAM **(b)** A bipolar RRAM.

2.5.2 Resistive switching mechanisms

The electrochemical metallization (ECM) effect is one of the RRAM switching mechanisms, the MIM cells consists of an electrode made from an electrochemically active metal M such as Ag, Cu, or Ni, an electrochemically inert electrode, such as Pt, Ir, W, or Au, and a thin film of a solid electrolyte ("I"), a M^{z+} ion-conductor which is sandwiched by electrodes. **Figure 2.10** shows the basic principle of operation of an ECM memory cell with an I-V switching cycle. At the beginning (**Figure 2.10d**), the Ag filament was not
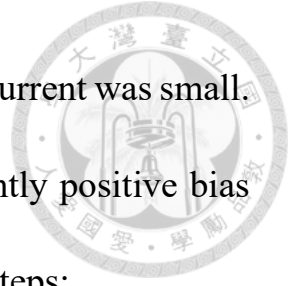
form, and the RRAM stayed at high resistance state, so the current was small.

A SET process occurs (**Figure 2.10a**) if applying sufficiently positive bias

voltage V. the overall SET process involves the following steps:

(1) the active electrode metal M at the insulator interface oxide to metal

cations M^{z+};

$$M \rightarrow M^{z+} + z\,e^- \tag{2.17}$$

(2) migration of the M^{z+} cations across the insulating film due to the high

electric field;

(3) reduction and electrocrystalliztion of M on the surface of the inert

electrode;

$$M^{z+} + z\,e^- \rightarrow M \tag{2.17}$$

The metal filament network will be formed at a SET process, once the

filament contact to active electrode and the two electrode connect to each

other, the RRAM will turn to ON state (**Figure 2.10b**). the RESET process

is shown in **Figure 2.10c**. The cell remains at ON state unless applying

sufficient voltage of opposite polarity, the electrochemical dissolution of the

metal filament makes the two electrode being not connected, then the RRAM

resets to high resistance state again.
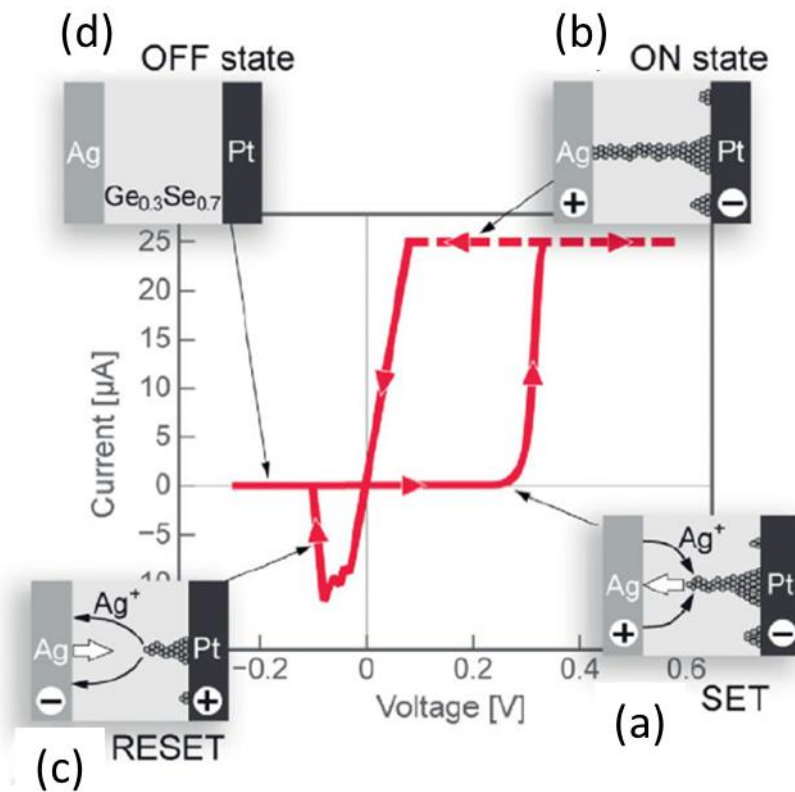
Figure 2.10 Resistive switching mechanisms. The electrochemical metallization effect (a) SET process **(b)** ON state **(c)** RESET process **(d)** OFF state

2.6 Magnetoelectronic device

2.6.1 Flexible electronics

In the future, electronic devices are desired to be more compact and portable. To achieve this purpose, the flexible electronics are developed proactively. There has been enormous progress in the materials, designs, and manufacturing processes for flexible system at present time. Flexible

28

electronics can be used in environmental monitoring, implants, display, pressure sensor, even in wearable device which can be applied in health monitoring[9-11].
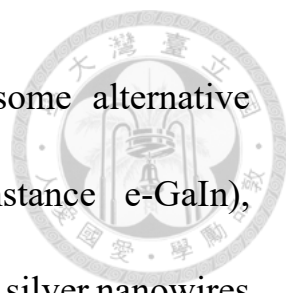
The flexible electronics need to bear mechanical deformation and to be reversible. There are some suitable materials to be a substrate materials for flexible applications: flexible glass, organic polymers (plastics), and metals.

Flexible glass - When the thickness of plate glass is reduced to several hundred μm, the glass will be flexible. Although the flexible glass is fragile and difficult to handle, it still remains all advantages of glass.

Organic polymer – Organic polymer substrates are highly flexible and inexpensive. However, the stability of polymer substrate under thermal condition and the resistance to chemicals is worse than glass substrate.

Metal foil – If the thickness of metal foil substrate is less than 125 μm, the metal foil will be flexible and can be an attractive substrate for emissive or reflective displays. Metals tend to be relatively resistive to temperature and most solvents. but their weight is a disadvantage, and they are more expensive but less flexible than plastic substrates.[11,12]

Metals are good electrical conductors and capable of withstanding modest bending-mode deformations. However, under large scale bending, metal

29

films are usually mechanically inadequate. There are some alternative materials can be used: electrical conductors (for instance e-GaIn), conducting nanowires (including carbon nanotubes (CNTs), silver nanowires and cooper nanowires), graphene, and conjugated polymers (such as PEDOT:PSS).[12] And the organic semiconductor are the important components of most flexible electronic devices, they can be dissolved in solution for flexible electronic applications.

2.6.2 The stretchable resistive sensor

A stretchable resistive sensor is a flexible substrate with patterned arrays of microstructures and the electrode is coated on the surface. The principle is the resistance of device will change due to the geometrical deformation of the microstructure[13-16]. There are various types of the patterned arrays on substrate; nanofiber, micropillar, microline, micropyramid structure are applied in the sensor.[13,14,17] In this thesis we used PDMS with the micropyramid array structure as the substrate and sprayed coating AgNWs on the micropyramid structure.

If the electrode of the micropyramid structure contact with a counter electrode, which depends on the degree of the contact, forming different
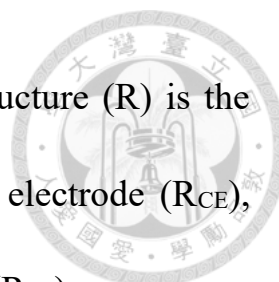
resistances. The resultant resistance around a pyramid structure (R) is the sum of three components: the resistances of the counter electrode (R_{CE}), contact interface (R_{CI}), and electrode of pyramid structure (R_{PE})

$$R = R_{CE} + R_{CI} + R_{PE} \qquad (2.17)$$

Because the resistance of counter is relatively low, Equation 2.17 can be described as $R \approx R_{CI} + R_{PE}$. Furthermore, R_{CI} and R_{PE} is influenced by resistivity (ρ), the contact area (A_{CI}), contact interface (D_{PE}). The resultant resistance can be expressed to be:

$$R = \frac{\rho_{CI} L_{CI}}{A_{CI}} + \frac{\rho_{PE} L_{PE}}{D_{PE} W_{PE}} \qquad (2.18)$$

Therefore, if the contact area (A_{CI}) is large, resultant resistance will be small.
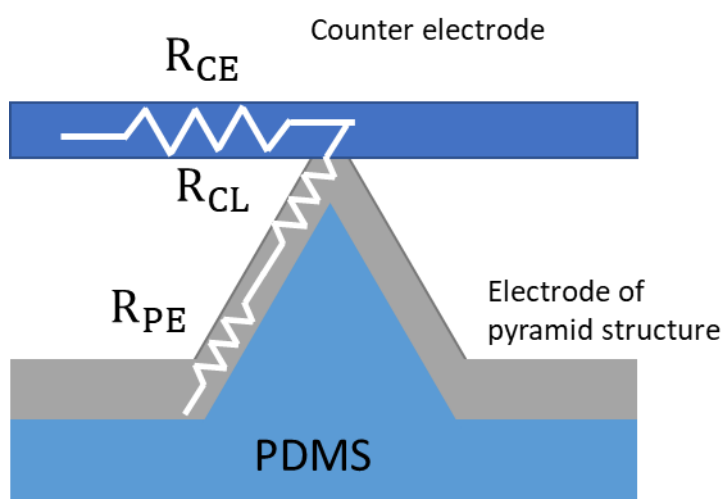
Figure 2.11 The schematic diagram of entire resistance composition.

Reference

1. https://en.wikipedia.org/wiki/Air_mass_(solar_energy)

2. https://www.laserfocusworld.com/lasers-sources/article/16566681/photovoltaics-measuring-the-sun

3. https://www.pveducation.org/pvcdrom/appendices/standard-solar-spectra

4. Banerji A, Tausch MW, Scherf U. Classroom experiments and teaching materials on OLEDs with semiconducting polymers. *Educ. Quim.* **24**, 17-22 (2013)

5. Tress W. *Organic solar cells: Theory, Experiment, and device simulation.* Springer International Publishing (2014)

6. Steim, R., Kogler, F. R., & Brabec, C. J. Interface materials for organic solar cells. *J.Mater. Chem.,* 20(13), 2499-2512 (2010)

7. Lin WP, Liu SJ, Gong T, Zhao Q, Huang W. Polymer-based resistive memory materials and devices. *Adv. Mater.* **26**,570-606 (2014).

8. Waser R, Dittmann R, Staikov G, Redoxed-based resistive switching memories-nanoionic mechanisms, prospects, and challenges. *Adv. Mater.* 21, 2632-2663 (2009)

9. Flexible Electronic Devices Are The Future — Here's Why,

September, 2018, https://www.youngupstarts.com/2018/09/21/flexible-electronic-devices-are-the-future-heres-why/

10. Nathan, A., Ahnood, A.< Cole, M. T., Lee, S. Suzuki, Y. Hiralal, P., …& Haque, S. Flexible electronics: the next ubiquitous platform. *Proc. IEEE*, 100(Special Centennial Issue), 1486-1517 (2012)

11. Wong, W. S., & Salleo, A. (Eds.). Flexible electronics: materials and applications (Vol.11). Springer Science & Business Media. (2009)

12. Harris, K. D., Elias, A. L. & Chung, H. J. Flexible electronics under strain: a review of mechanical characterization and durability enhancement strategies. *J. Mater. Sci.,* 51(6), 2771-2805 (2016)

13. Choong, C. L., Shim, M. B., Lee, B. S., Jeon, S., Ko, D. S., Kang, T. H., … & Jeong, Y. J. Highly stretchable resistive pressure sensors using a conductive elastomeric composite on a micropyramid array. *Adv. Mater.,* 26(21), 3451-3458 (2014).

14. Fa, F. R., Lin, L., Zhu, G., Wu, W., Zhang, R., & Wang, Z. L. Transparent triboelectric nanogenerators and self-powered pressure sensors based on micropatterned plastic films. *Nano Lett.,* 14(14), 1704232 (2018).

15. Kim, K. H. Jang, N. S., Ha, S. H., Cho, J. H., &Kim, J. M. Highly

sensitive and stretchable resistive strain sensors based on microstructured metal nanowire/elastomer composite films, *Small,* 14(14), 1704232 (2018).

16. Mannsfeld, S. C., Tee, B. C., Stoltenberg, R. M., Chen, C. V. H., Barman, S., Muir, B. V., … & Bao, Z. Highly sensitive flexible pressure sensors with microstructured rubber dielectric layers. *Nat. Mater.*, 11(9), 795 (2012)

17. Pang, C., Lee, G. Y., Kim, T. I., Kim, S. M., Kim, H. N., Ahn, S. H., & Suh, K. Y. A flexible and highly sensitive strain-gauge sensor using reversible interlocking of nanofiber. *Nat Mater.,* 9(10), 795 (2012)

Chapter 3　Experimental details

3.1 Instrument

3.1.1 The list of equipment

Instrument	Manufacturer	No.
Multimeter	Keithley	Keithley2400
Solar simulator	Newport Inc.	91195A&69920
White light led	Mightex Systems	LCS-6500-15-22
Function generator	Tektronix	AFG3101
Oscilloscope	Agilent	DSO5054A
Scanning electron microscope (SEM)	JEOL	SM-6700F

3.1.2 Scanning electron microscope (SEM)

The scanning electron microscope is a type of microscope which can produce images by scanning surface of the sample with focused electrons beam. After passing through series electromagnetic lenses, the high-energy electron beam of SEM can be focused onto the sample. These electrons interact with atoms in the sample and release the elections on the surface. According to Abbe's law:

$$d \geq \frac{0.61\lambda}{n\sin\alpha} \tag{3.1}$$

where d is distinguishable distance, n is the refraction index of the medium, α is the half angle of the light cone, λ is the wavelength of the light. Due to the short material wave length of the high energy electron, the resolution of the SEM can achieve to nanometer scale.

Figure 3.1 shows the SEM instrument (JEOL,JSM-6500F) we use to produce images. It uses Schottky type field-emission gun (tungsten coated with ZrO_2) as electron beam source with a probe-current from 10 pA to 20 nA and electron energy level ranging from 5 to 30 keV.

36

Figure 3.1 Scanning electron microscope

3.1.3 Solar simulator

Solar simulator is an instrument providing illumination to stimulate natural solar spectrum on the earth surface, The purpose of solar simulator is to provide an imitate facility for testing solar cells under laboratory condition. The current density-voltage (J-V) characteristic curves of solar cells are measured by Keithley Model 2400 source meter which is controlled by Labview program to generate bias voltage. The illumination spectrum is provided by an Oriel Class A solar simulator which is equipped with AM1.5G filter. The light intensity of the system measurement is 1000 W/m^2, which is calibrated by NREL reference cell.
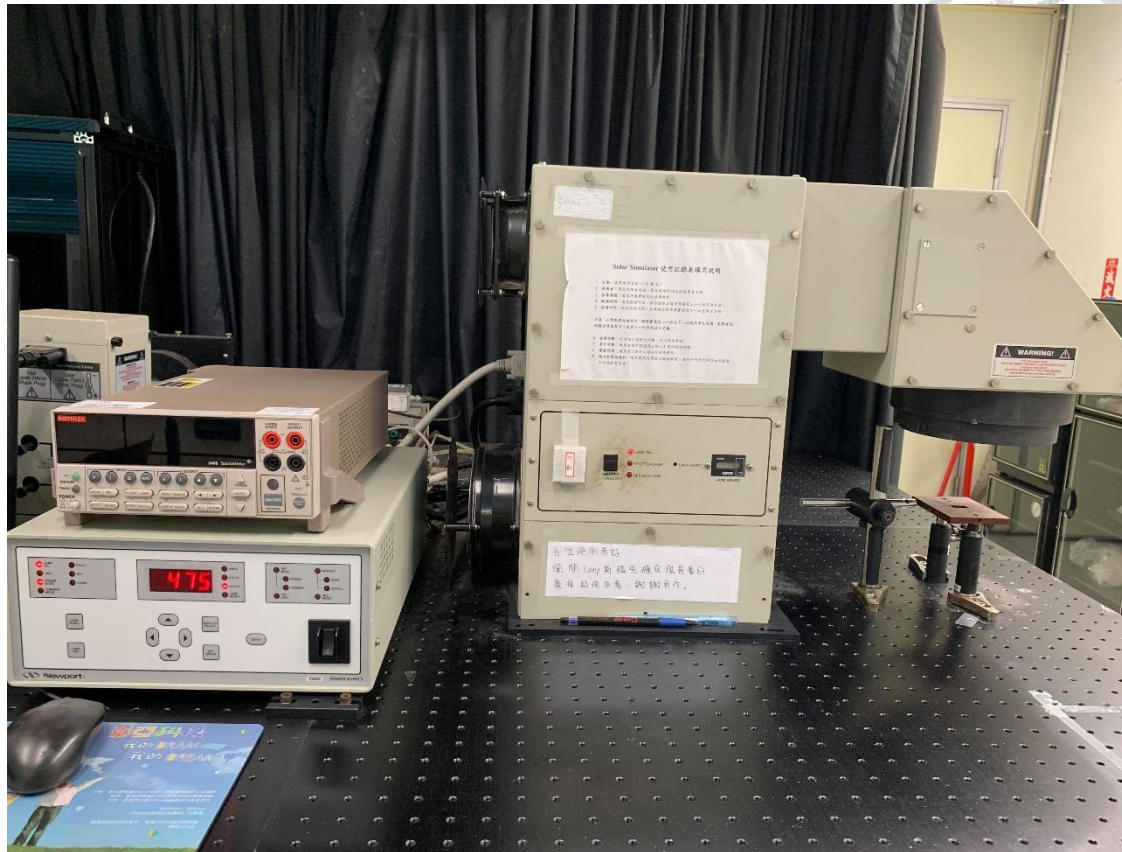
Figure 3.2 Solar simulator and Keithley 2400.

3.1.4 Thermal evaporation

Thermal evaporation is a common method of thin film deposition. The principle of the thermal evaporation is heating the source material by the resistance and evaporate it. Because thermal evaporation process works in at about 10^{-6} torr which is in high level, the mean free path is long enough to avoid reaction between the vapor and atmosphere. At these low pressures, these vapor particle may travel straightly from the evaporation source to the substrate.

38

Figure 3.3 Thermal evaporation system.

3.2 Materials

3.2.1 The list of materials

Material	Chemical formula	Manufacture	No.
ITO-Glass		FMPV	OAST0007-0050
Zinc Acetate Dihydrate	$Zn(CH_3COO)_2 \cdot 2H_2O$	J.T Baker	4296-01 Zinc Acetate Dihydrate,Crystal ,BAKER ANALYZED^{TM} ACS Reagent Grade
2-methoxyethanol	$CH_3OCH_2CH_2OH$		
ethanolamine	$NH_2CH_2CH_2OH$	ACROS	Ethanolamine, 99%
Poly (3-hexylthiophene) (P3HT)	$(C_{10}H_{14}S)_n$	FMPV	P3HT 49K
[6,6]-phenyl-C_{61}-Butyric acid methyl ester (PC$_{61}$BM)	$C_{72}H_{14}O_2$	LUMTEC	LT-S905
O-Dichlorobenzene (O-DCB, DCB)	$C_6H_4Cl_2$	ACROS	O-DCB >98%
Molybdenum(VI) oxide	MoO_3	Alfa Aesar	Molybdenum(VI) Oxide >99.95%
Silver	Ag	Gredmann	Ag 99.99%
Gold	Au	Gredmann	Au 99.99%
Poly(methyl methacrylate)	$(C_5H_8O_2)_n$	Microchem	950 PMMA A6

(PMMA)			
Silver nanowires	AgNWs	KECHUANG	AW030
Polydimethylsiloxane (PDMS)	$(C_2H_6OSi)_n$	Dow Corning (DOWSIL)	Sylgard 184 Silicone Elastomer
Iron-Nickel alloy	Fe-Ni alloy	Gredmann	

3.2.2 Poly(3-hexylthiophene) (P3HT)

Poly(3-hexylthiophene) (P3HT) is a conjugated polymer which is often used in organic electronics. It is usually be a donor polymer in organic photovoltaics with its HOMO 5.1eV and LUMO 3.1eV. The absorption range of P3HT is about from 350 nm to 700 nm
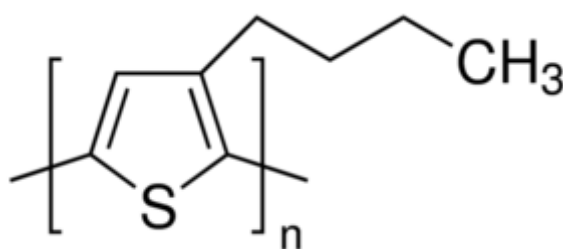
Figure 3.4 Chemical structure of P3HT

3.2.2 [6,6]-phenyl-C_{61}-Butyric acid methyl ester ($PC_{61}BM$)

[6,6]-phenyl-C_{61}-Butyric acid methyl ester ($PC_{61}BM$) is a derivative of fullerene C_{60} which has great solubility in common solvent. its HOMO and LUMO 6.0 eV and 4.3 eV, respectively making it to be used as an acceptor

41

in organic photovoltaics.
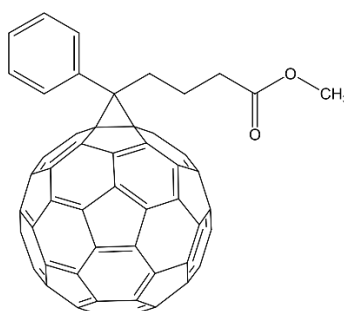
Figure 3.5 Chemical structure of $PC_{61}BM$

3.2.4 Poly(methyl methacrylate) (PMMA)

Poly(methyl methacrylate) (PMMA), which is also known as acrylic or acrylic glass, is a transparent organic polymer and is often used as a photoresist in the semiconductor fabrication. Because of its high resistance, it used as an insulator layer material in this work.
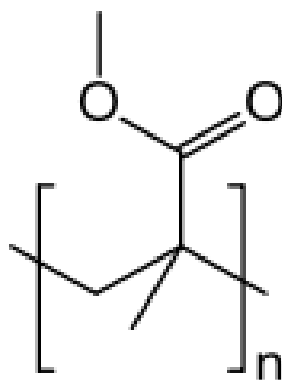
Figure 3.6 Chemical structure of PMMA

3.2.5 Polydimethylsiloxane (PDMS)

Polydimethylsiloxane(PDMS) is a silicon-based organic polymer which is has widely used. PDMS has many unique physical and chemical properties,

such as flexible, thermo-tolerant, resistance to oxidation, easy fabrication, tunable hardness, optical transparency, etc. PDMS acts like a viscous liquid or an elastic solid under different situation. We usually use cross-linking agent turning it into elastic solid.
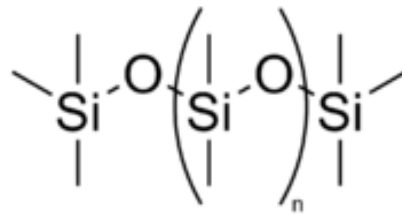
Figure 3.7 Chemical structure of PDMS

3.2.6 Silver nanowires (AgNWs)

Silver nanowires (AgNWs) has the highest conductivity of all metals. Moreover, AgNWs can form an transparent and flexible electrode. In this study, the average diameter and average length of AgNWs is 25~35 nm and 20~40 μm.

3.3 Material preparation

3.3.1 Preparation of ITO glass

The glass we use is prepatterned by the transparent electrode indium doped in oxide film, the resistance of which is 15 Ω/sq. These ITO-glasses are cleaned in soap water for 30 minutes, then cleaned in DI water, acetone

and ethanol tandemly for 15 minutes pre step.

3.3.2 Preparation of Sol-gel-derived ZnO

500 mg Zinc acetate dihydrate ($Zn(CH_3COO)_2 \cdot 2H_2O$) and 139 mg ethanolamine ($NH_2CH_2CH_2OH$) are dissolved in 5 mL 2-methoxyethanol ($CH_3OCH_2CH_2OH$) and stirring for 12 hours for the hydrolysis reaction in the air.

3.3.3 Preparation of P3HT: $PC_{61}BM$ solution

The active layer is a mixture of P3HT and $PC_{61}BM$ which were dissolved in O-Dichlorobenzene (ODCB) solvent with D/A ratio of 1:1 and con centration 40 mg/ml. The solution is stirring under 50°C and 500 rpm overnight. Before spin coating, the active layer solution need to be filtted by 0.45 μm PTFE syringe filter.

3.4 Device fabrication

3.3.1 Organic solar cells

A 30 nm thick ZnO film was deposited on the ITO glass by spin coating sol-gel ZnO solution with 4000 rpm for 40 sec. After that, annealing at 200°C for 1 hour. Then depositing active layer on the ZnO film by spin coating the

44

mixture of P3HT:PC$_{61}$BM (D/A ratio 1:1) at 800 rpm 40 s, in air. Then thermally evaporating MoO$_3$ (7nm) as a hole transport layer, following depositing Ag (100 nm)by thermal evaperation.

3.3.2 RRAM cells

The PMMA solution was spun on the top of the cleaned ITO-glass at 5000 rpm for 50 s. Then, the thermal deposition of Ag (100 nm) layers was carried out on the PMMA layer completing the device fabrication.

3.3.3 Flexible magnetoelectronic device

For the preparation of the flexible magnetoelectronic device, a two-component reagent is used. The siloxane base was mixed with cross-linking agent at the weight ratio of 10:1. Then, adding the powder of Fe-Ni alloy into above mixture with 33 wt %. After that, degassing under vacuum for 30 minutes. The mold with the microstructured surface was made from <100> silicon wafers (300 nm- SiO$_2$) by wet etching. Spin-coating the mixture on the mold with 600 rpm for 10 s. The mixture on the mold was cured at 70℃ for an hour in an oven. After curing, the elastomer of periodic nanopyramid structures was peeled off from the mold. Finally spray coating AgNWs IPA

45

solution with concentration of 0.5 mg/ml on the Fe-Ni/PDMS film.

3.3.4 Phototransistor

A 30 nm thick ZnO film was deposited on the ITO glass by spin coating sol-gel ZnO solution with 4000 rpm for 40 sec. After that, annealing at 200℃ for 1 hour. Then depositing active layer on the ZnO film by spin coating the mixture of P3HT:PC$_{61}$BM (D/A ratio 1:1) at 800 rpm 40 s, in air. Then thermally evaporating MoO$_3$ (7nm) as a hole transport layer, following depositing Ag (100 nm) by thermal evaporation. For RRAM part, the PMMA solution was spun on the top of ITO/ZnO/ P3HT:PC$_{61}$BM/ MoO$_3$/Ag at 1500 rpm for 50 s. Then, the thermal deposition of Au (80 nm) layers was carried out on the PMMA layer completing the device fabrication.

Reference

1. C.Y . Tzou, S. Y. Cai, C. Y. Tseng, C. Y. Chang, S. Y. Chiang, C. Y. Jiang, Y. H. Li, J. M. Ma, Y. M. Liao, F. C. Hsu, Y. F. Chen, An ultra-fast two-terminal organic phototransistor with vertical topology for information technologies. Appl. Phys. Lett., 114(19) 193301 (2019).

2. S. Y. Cai, C. H. Chang, H. I. Lin, Y. F. Huang, W. J. Lin, S. Y. Lin, Y. R. Liou, T. L. Shen, Y. H. Huang, P. W. Tsao, C. Y. Tzou, Y. M. Liao, and Y. F. Chen, Ultrahigh sensitive and flexible magnetoelectronics with magnetic nanocomposites: Toward an additional perception of artificial intelligence. ACS Appl. Mater. Interfaces, 10(20) 17393-17400 (2018).

3. C. Y. Jiang, C. H. Tsai, C. Y. Tzou, F. C. Hsu, and Y. F. Chen. Magnetically controllable and flexible phototransistors for artificial intelligent skin with additional perception. Organic Electronics 85 105849 (2020).

4. https://en.wikipedia.org/wiki/Polydimethylsiloxane

5. https://en.wikipedia.org/wiki/Poly(methyl_methacrylate)

Chapter 4　Results and Discussion

4.1 Characteristics of resistive random access memory

The RRAM cell structure is ITO/PMMA/Ag, and the working area defined by the overlapping area between two electrode is 0.04 cm^2. ITO was grounded and voltage was applied from Ag electrode. **Figure 4.1a** shows the characteristic curves of RRAM cells. At V < +1.2 V, because the Ag filament was not formed in the PMMA layer, the RRAM cell was in the high resistance state, or OFF state. When the applied bias exceeds the set voltage (about +1.2 V), the Ag filament was formed and connected two electrodes, the RRAM cell changed to low resistance state, or ON state. The current rapidly increased and reached to compliance current (C.C.). When the reverse bias was large enough, the Ag filament would break. The current dramatically decreased and the RRAM was switched to the OFF state again. **Figure 4.1b** shows the 50 switching cycles of the ON and OFF state at reading voltage of +0.5V. It indicates that the RRAM device possesses excellent endurance.
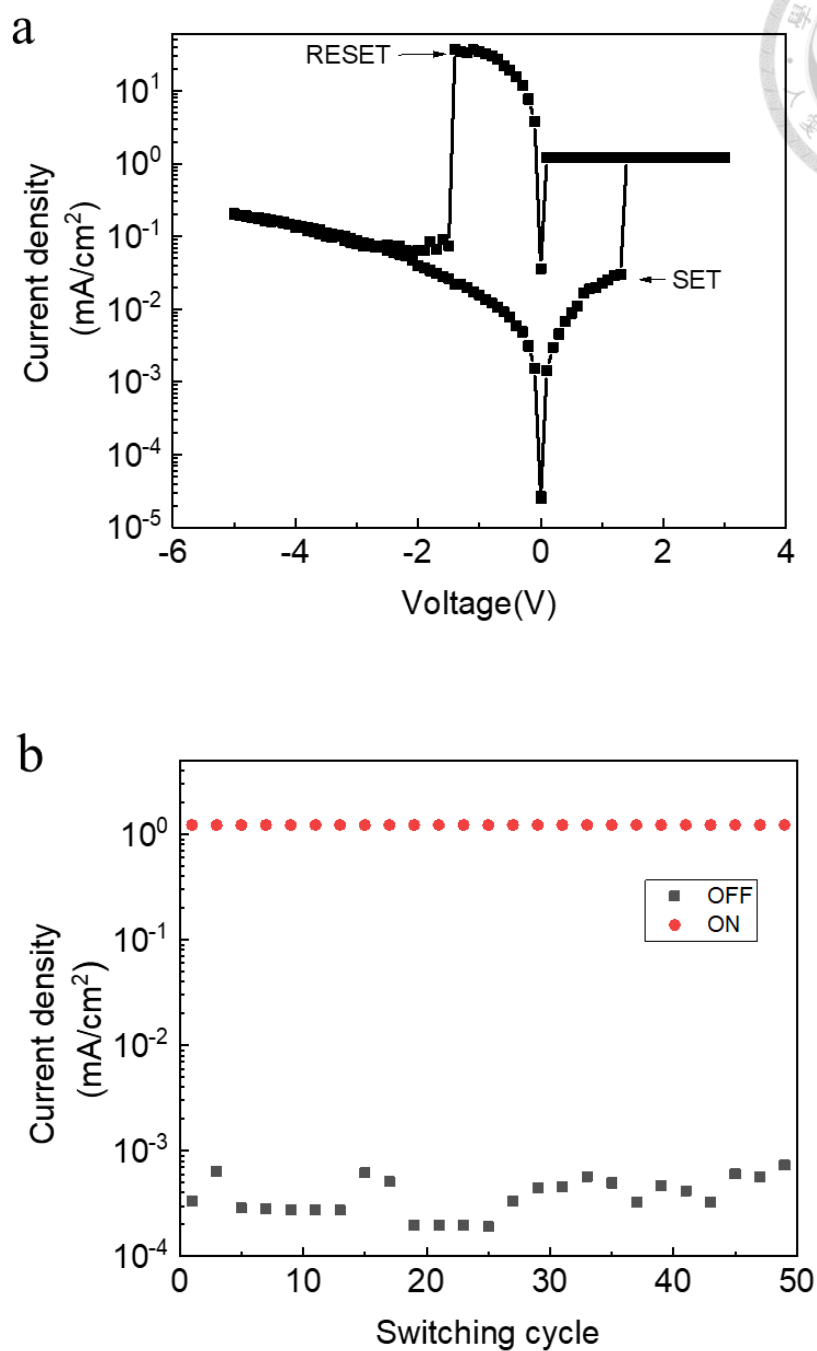
Figure 4.1 Device performance of ITO/PMMA/Ag memory. (a) *J-V* characteristic of ITO/PMMA/Ag memory. **(b)** ON/OFF switching for 50 cycles at + 0.5V

4.2 Characteristics of organic solar cell

The organic solar cell is of layered structure of ITO/ZnO/ P3HT:PC_{61}BM/ MoO_3/Ag, and the working area defined by the overlapping area between two electrode is 0.04 cm^2. **Figure 4.2a** shows the current density verses voltage (*J-V*) characteristic curve of organic solar cell under one sun AM 1.5G illumination. Short circuit current density *(J_{sc})*, open circuit voltage *(V_{oc})*, fill factor (FF), and the power conversion efficiency (PCE) are 12.077 mA/cm^2, 0.539 V 61.17%, and 3.98%, respectively. To measure the characteristic of the device under different light intensity, we used white light LED as a light source in this study. **Figure 4.2c** shows the emission spectrum of white light LED. And **Figures 4.2b and d** show the (*J-V)* characteristic curves of the organic solar cell under different optical intensity. According to the curves, we can find that the photocurrent increases as the light intensity increases.
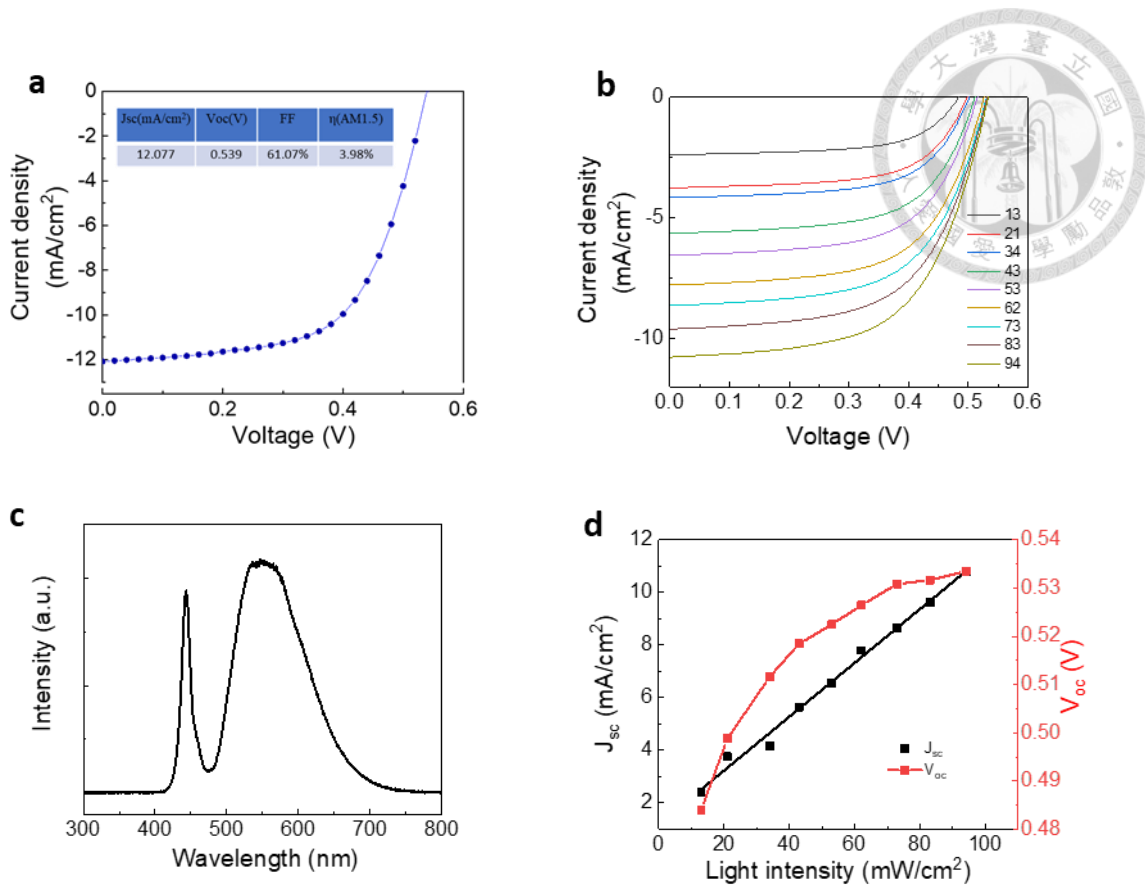
Figure 4.2 (a) *J-V* characteristic curve and parameters of solar cell under one sun with AM1.5G filter. **(b)** *J-V* characteristic curves of solar cell under different light intensities. **(c)** The spectrum of the white light LED. **(d)** The short circuit current density (J_{sc}) and the open circuit voltage (V_{oc}) in different light intensities.

51

4.3 Characteristics of flexible magnetoelectronic device

The magnetic response of the magnetoelectronic device is presented in **Fig. 4.3a** showing the current responses of the device under different magnetic fields at operating voltage of +0.1 V. When the magnetic field is larger than the threshold field of 70 mT, the magneto-electronic film and ITO electrode can contact each other and allow current larger than the threshold current (I_0) of 2.1×10^{-4} mA flowing through. It is known that the sensitivity of this device is defined as

$$S = \frac{\Delta I}{I_0} \cdot \frac{1}{\Delta B} \qquad (4.1)$$

where ΔI is the change of the response current, and ΔB is the change of the applied magnetic field. To calculate the sensitivity of the magnetoelectronic device under distinct magnetic fields, we replotted the data and the result as shown in **Fig. 4.3b**. Apparently, there are three different slopes of the current response, which represent three different sensitivity. In the low magnetic field region (below 93 mT), because of the small contact area between micropyramid structure and ITO electrode, the sensitivity is $69.69\% \, \mathrm{mT^{-1}}$, which is relatively low. As magnetic field gets stronger (from 123 mT to 213 mT), the sensitivity increases significantly to $2989.57\% \, \mathrm{mT^{-1}}$ due to the large deformation of micropyarmid structure.
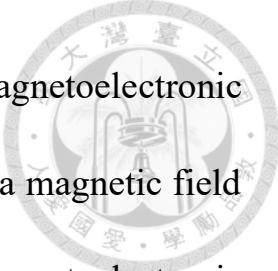
For further increasing magnetic field (above 233 mT), there is only a slight increment of $1010.33\%\ mT^{-1}$, which can be attributed to approaching the deformation limit of the PDMS micropyramid. Based on the magnetic response property, the magnetoelectronic device can function as a switch and a tuner, whose output current is tunable by different magnetic field.
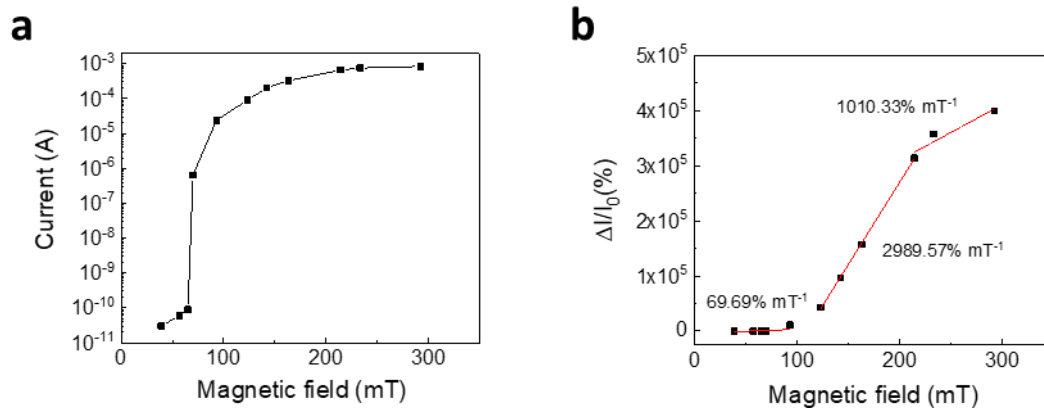
Figure 4.3 (a) The current response versus different magnetic fields at operating voltage of +0.1 V. **(b)** The sensitivity of the flexible magnetoelectronic device.

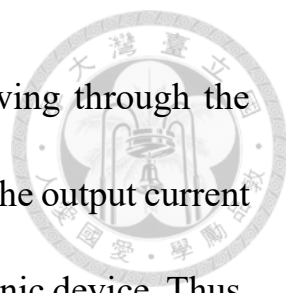## 4.4 Characteristics of the dual-gate phototransistor

Figure 4.4a displays the schematic diagram of the double-gate phototransistor, which is composed of an ITO/ZnO/ P3HT:P C_{61} BM/ MoO_3 /Ag organic solar cell (OSC) in tandem with a Ag/PMMA/Au resistive random access memory (RRAM) under a FeNi/PDMS/AgNWs magnetoelectronic film 80 μm away defined by a PET film. Figure 1(b) displays the top-view SEM image of a micro-pyramid structure film with AgNWs, showing the average dimensions of 15 μm × 15 μm × 7.8 μm for a single micro-pyramid. The FeNi/PDMS/AgNWs structure uses the Au layer of the bottom RRAM to serve as its second electrode to form a magnetoelectronic device of layered structure of FeNi/PDMS/AgNWs/ air gap/Au. Stacking a magnetoelectronic film and RRAM structure on the top of an OSC resulting in an intriguing type of dual-gate transistor, which can sense optical, electrical and magnetic stimuli and respond accordingly. **Figure 4.4c** shows the equivalent circuit of the dual-gate phototransistor. There are three parts of the transistor: photonic part, electric part and magnetic part. For the photonic part, when the light irradiates on the OSC, photons are absorbed and converted to electron hole pairs to generate current. In the electric part, we connect ITO electrode to the

ground and apply sufficient negative/positive bias on the magnetoelectronic film to control the status of RRAM. For the magnetic part, a magnetic field greater than 70 mT can determine the contact extent of the magnetoelectronic device. In the dark, the set and reset voltage to turn on the RAMM component is magnetic field dependent. **Figure 4.4d** displays the typical current density (J) – voltage (V) characteristics of phototransistor. ITO was grounded and the potential was applied on the magnetoelectronic device. A single RRAM had the set and reset voltages of -1.2 V and $+1.4$ V, respectively. Under a constant magnetic field of 120 mT, the set and reset voltages of the phototransistor increased to -2.6 V and $+2.5$ V, respectively, to turn the device ON and OFF. After further increasing the applied magnetic field to 250 mT, the set and reset voltages dropped to -1.6 V and $+1.8$ V, respectively. The shift of the electric setting voltages originates from the resistance of OSC and the magnetic field dependent contact resistance of the magneto-electronic component (**Figure 4.3** for details).
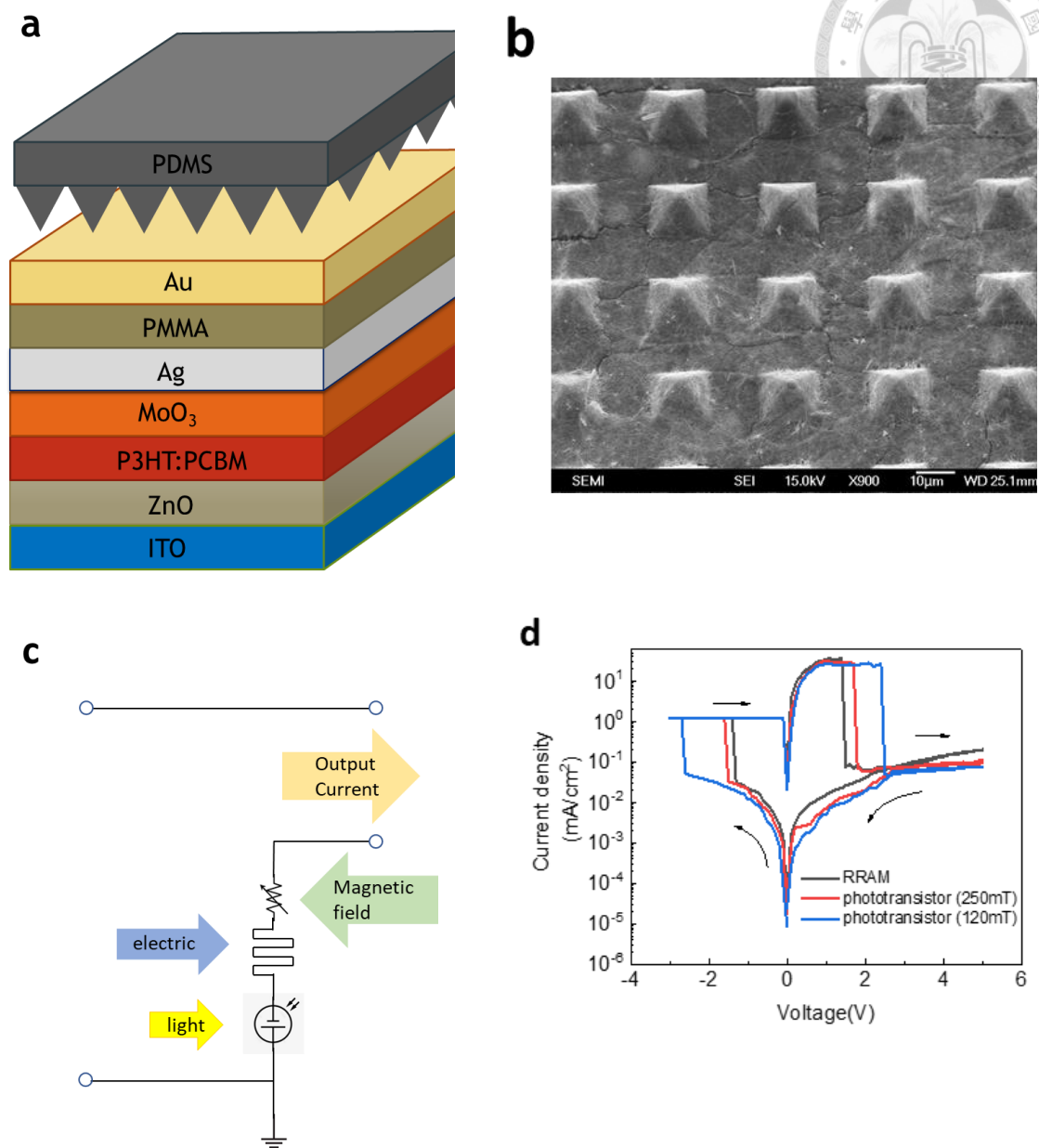
Figure 4.4(a) Schematic device structure of the double-gate phototransistor. **(b)** The top view SEM image of the micropyramid film covered with AgNWs. **(c)** The equivalent circuit of the double-gate phototransistor. **(d)** The electrical switching curves of the phototransistor under different magnetic fields in the dark.

When light illuminates, OSC will generate current flowing through the RRAM and magnetoelectronic device, and one can control the output current by varying the ON/OFF state of RRAM and magnetoelectronic device. Thus, both RRAM and magnetoelectronic device function as the gate electrode in a conventional dual-gate field effect transistor. We define the current density of the phototransistor as the output signal. **Figure 4.5** shows operation of the dual-gate transistor at operation voltage of 0 V. By keeping light intensity at 40.8 mW/cm^2 from a white light LED, we varied the status of RRAM under a specific state of the magnetoelectronic device and vice versa. In $5 \sim 40$ s, initially, we applied -5 V to turn on RRAM, and varied external magnetic field between 0 and 330 mT and the output of the phototransistor response accordingly ; i.e., zero current output at 0 T and -5 mA/cm^2 (compliance current density) at 330 mT. For the following $35 \sim 70$ s, we kept the external magnetic field at 330 mT and changed the state of RRAM by applying alternative voltage of $+5$ V and -5 V to turn OFF and ON the device. As expected, the phototransistor can only have output current in the ON state of RRAM. For the rest time periods of 71~100 s and 100~140 s, the magnetic field was set to 0 T and RRAM was turned off, respectively, and no output current was obtained from the phototransistor by varying the
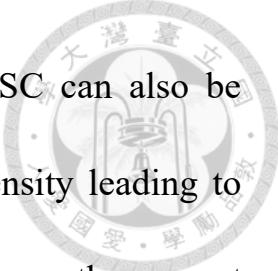
57

other stimuli. In a sense, both the RRAM and magnetoelectronic device work as switches, which can control the photocurrent output from phototransistor. Thus, the role of RRAM and magnetoelectronic device is similar to the gate electrode in a conventional field effect transistor.
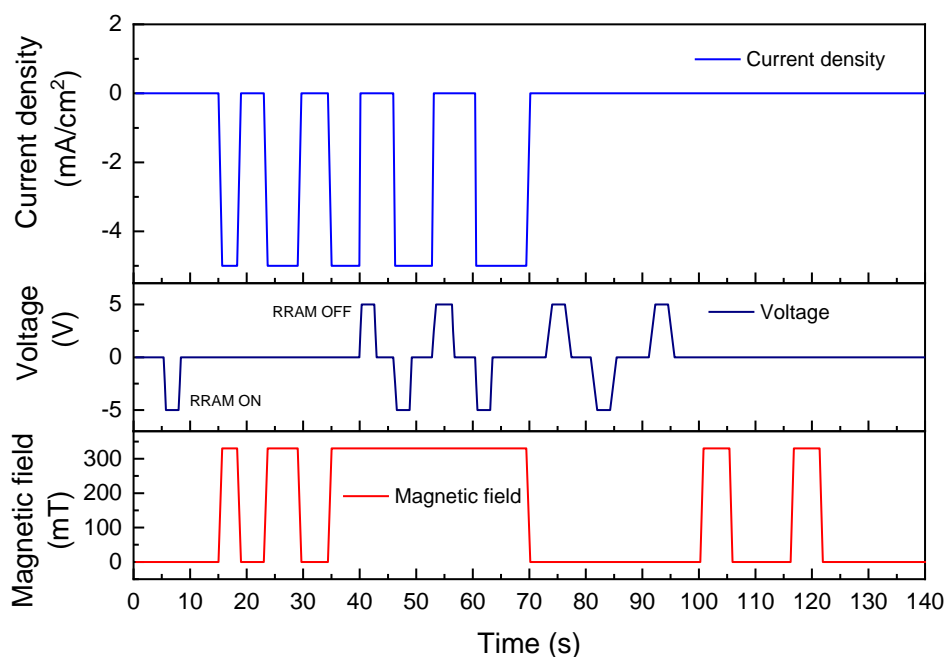
Figure 4.5 Operation of the double-gate phototransistor under the light intensity of 40.8 mW/cm^2.
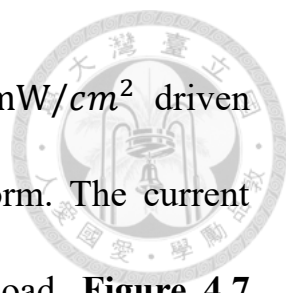
In addition to RRAM and magnetoelectronic device, OSC can also be controlled in ON and OFF states by controlling light intensity leading to eight working states of the phototransistor. **Figure 4.6** shows the current density versus voltage (J-V) curves measured from -0.2 V to 0.8 V in different working states. **Figures 4.6(a) and (b)** show the working states under a constant magnetic field of 330 mT and the output of the phototransistor is a diode (photodiode) curve when RRAM is in the ON state at light intensity of 0 (50) mW/cm^2. In **Figures 4.6(c) and (d),** because the magnetoelectronic device is at OFF state, there will not be any output current for the phototransistor irregardless the status of RRAM and OSC.
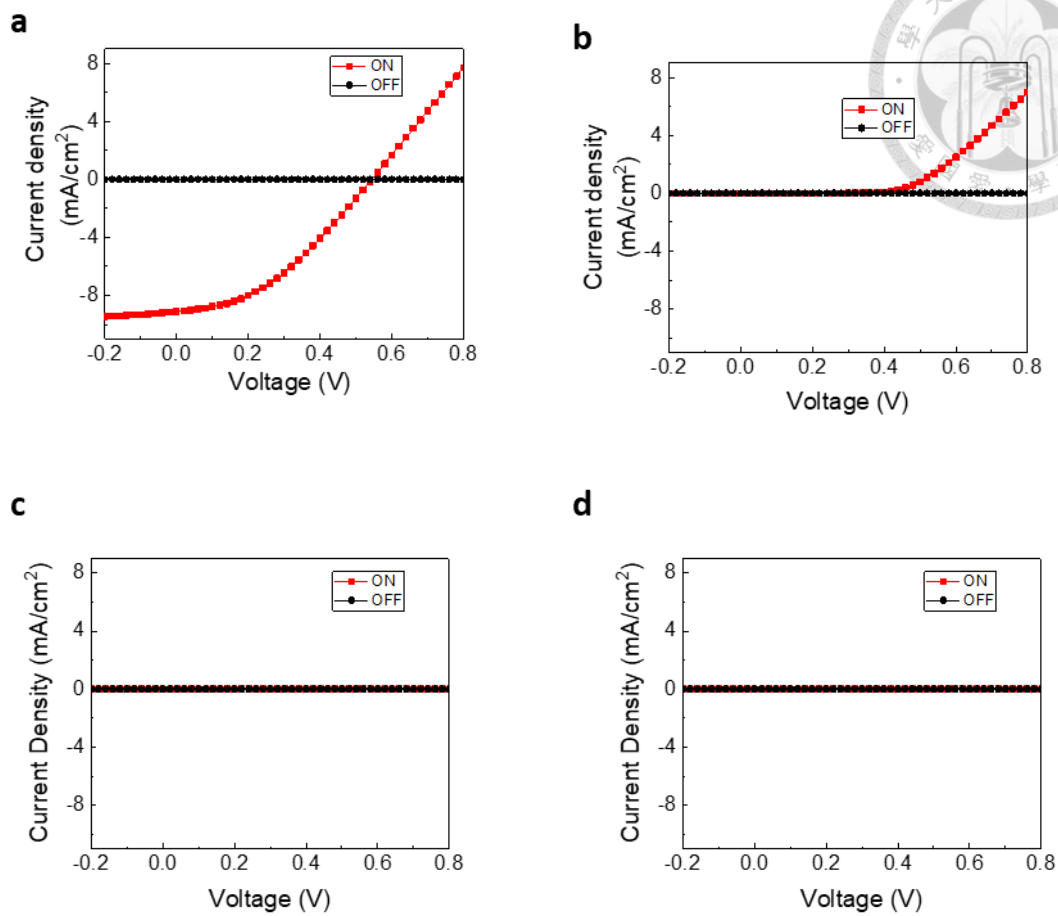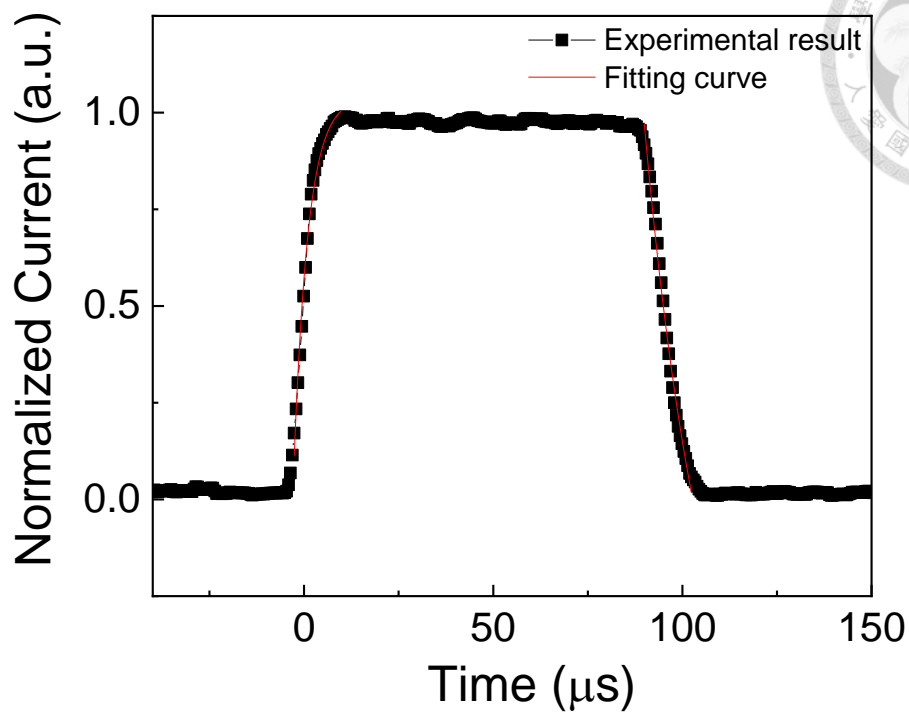
Figure 4.6 (a) *J-V* curves of the phototransistor at ON/OFF state of RRAM

under various light intensity, I (mW/cm^2) and magnetic field, B (mT),

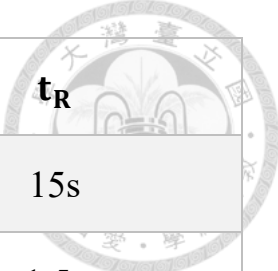(I, B) = **(a)** (50, 330) **(b)** (0, 330) **(c)** (50, 0) and **(d)** (0, 0)

Photoresponse is also an important parameter to characterize a

phototransistor. To measure the photoresponse of the device, we applied

reverse bias -5 V and magnetic field of 163 mT to set both RRAM and

magnetoelectronic device to ON state, respectively, and the device was

60

illuminated by a white light LED at an intensity of 40.8 mW/cm^2 driven by a function generator set to a 2.5 kHz square waveform. The current response was recorded by an oscilloscope with 50 Ω load. **Figure 4.7** displays the obtained photocurrent transient, which yields the rise time and the fall time of 3 μs and 6 μs, respectively, after fitting the transient current by the sample exponential function. **Table 4.1** shows the comparison of previous reported OPTs. Compared to organic phototransistors of lateral structure whose response time usually ranges from millisecond to second[1-9], our phototransistor responses much faster and is suitable to be a photodetector. The reasons for the fast response time can be attributed to the vertical layout configuration of the device and the bulk heterojunction structure for photon sensing. The channel length of the vertical configuration is shorter than that of the lateral structure. The bulk heterojunction structure can make photogenerated excitons spilt more efficiently due to the build-in electric field. As a result, an efficient exciton dissociation medium with shorter change travelling channel can improve photoresponse time.

Figure 4.7 The normalized photocurrent response of the phototransistor at

the light intensity of 40.8 mW/cm^2**,** yielding the rise time and fall time of

3 μs and 6 μs, respectively.

| Material	structure	t_R
A-EHDTT	Lateral	15s
Spiro-DPSP	Lateral	1.5s
4(HPBT)-benzene	Lateral	1s
Pentacene/PC_{61}BM	Lateral	210ms
P3HT:TiO_2	Lateral	200ms
Pentacene	Lateral	100ms
P3HT	Lateral	20ms
F_{16}CuPc	Lateral	10ms
MDMO-PPV:PC_{61}BM	Lateral	16µs
P3HT:PC_{61}BM	vertical	3µs

Table 4.1 Comparison of structure and response time of previously reported

organic phototransistor.

t_R is the device photoresponse time.

4.5 Demonstration of potential application
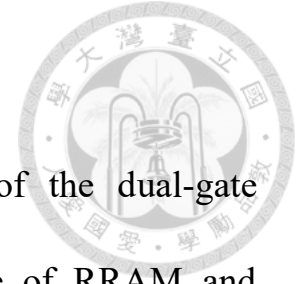
In **Figure 4.6**, we have demonstrated the output of the dual-gate phototransistor can be controlled by the ON/OFF state of RRAM and magnetoelectronic device. Following, we put forward an unprecedented application based on the hybrid control of the optical, electrical and magnetic stimuli to determine whether the small electrically input signal can be transported or not. We applied a positive square waveform of 0.25 V at 100 Hz as a small AC voltage signal (ΔV) and measured the output current change (ΔJ). The measuring circuit is shown in **Figure 4.8**. **Figure 4.9a** demonstrates that when RRAM is ON, the small signal can be transported and with an invert phase under a constant light illumination at 100 mW/cm^2 and magnetic field of 330 mT. For **Figures 4.9b-d**, regardless the state of RRAM, no small signal can be transported when either light or magnetic field is active. In a sense, the small voltage signal can be transported only when light, electric voltage, and magnetic field are active simultaneously; i.e., OSC, RRAM, and magnetoelectronic device are activated. Thus, this dual-gate phototransistor can be used as a logic element in an electric circuit. It can be understood as a series of a NOT gate and an ENABLE gate connected to an AND gate as the effective digital logic diagram shown in **Figure 4.9e.**

64
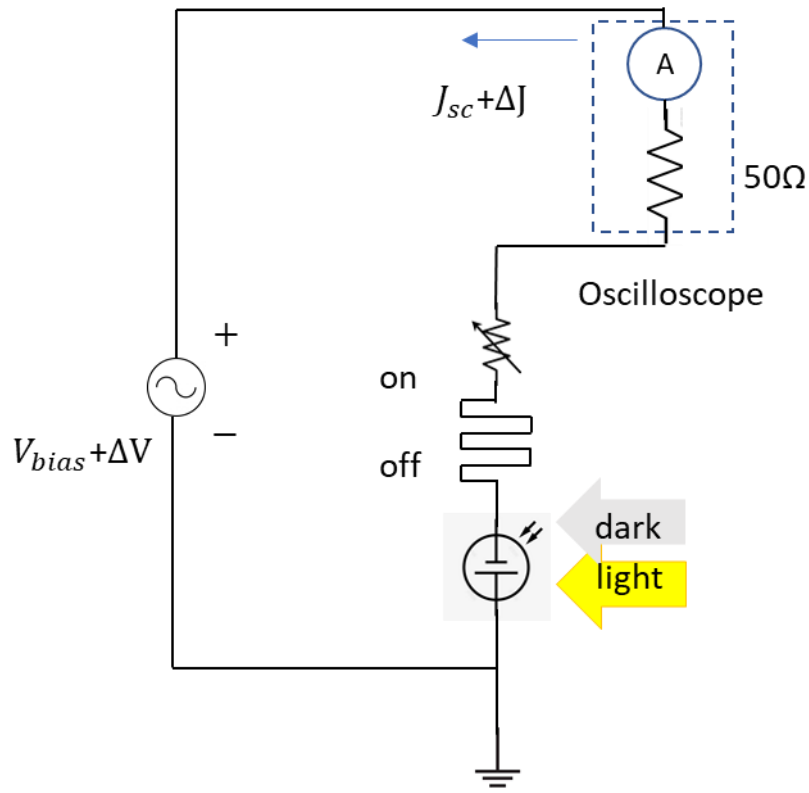
Figure 4.8 Working circuit of transporting small electrically input signal

(ΔV).
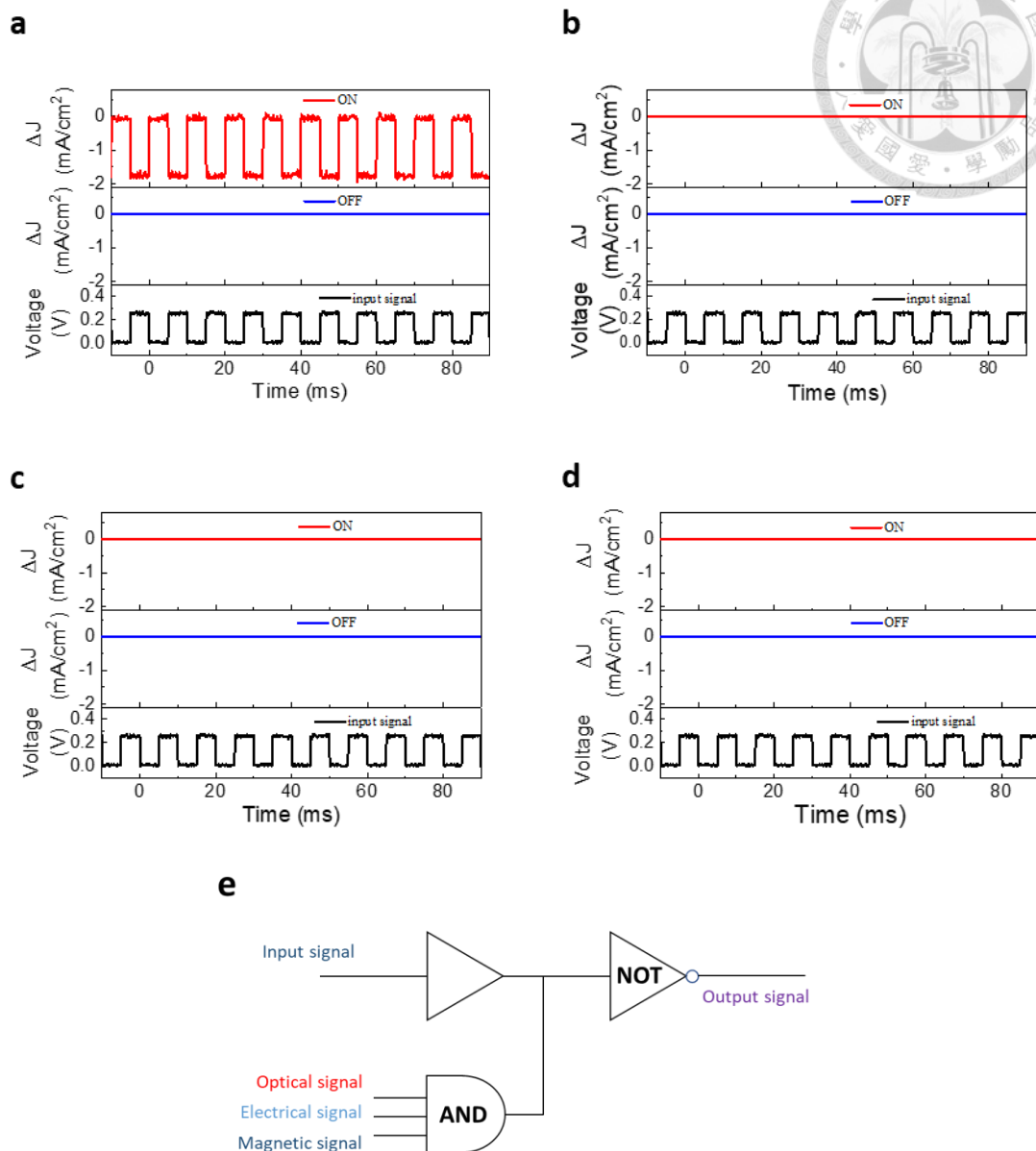
Figure 4.9 Demonstration of transporting small electrical signals via hybrid control of the optical, electrical and magnetic stimuli. The input positive square waveform signal (amplitude 0.25 V, frequency 100 Hz) and the output current change (ΔJ) in the ON/OFF state of RRAM under (a) I = 100 mW/cm^2, B = 330 mT ; (b) I = 0 mW/cm^2, B = 330 mT ; (c) I = 100 mW/cm^2,

B = 0 mT ; (d) I = 0 mW/cm^2, B = 0 mT ; (e) The effective digital logic diagram of the double-gate phototransistor.

Moreover, the output signals of both OSC and magnetoelectronic device can be modulated independently by controlling illuminating intensity and magnetic field, **Figures 4.10a and 4.10b** show modulation of the phototransistor output at different light intensities under 330 mT and various magnetic field strengths at constant light intensity of 10.76 mW/cm^2, respectively. It can be seen that the amplitude of the output signal scales with the varied stimuli in the ON state of RRAM. Since the state of RRAM is nonvolatile, one can also alter the operation voltage as well and the result is shown in **Figure 4.10c** under 330 mT and 1 sun. Based on this special digital logic characteristic, this dual-gate phototransistor can be functioned as triple-valve lock on the information stream. One can encrypt the data stream by encoding the combination of electrical, magnetic, and optical codes to the original information to create encrypted signal. For the receiver, it is inevitable to know the exact parameters for the illuminating intensity, voltage, and magnetic field to decrypt the data. Moreover, a new wireless

communication technology called Li-Fi has been proposed. Li-Fi has numerous advantages such as wider channel bandwidth and faster transition speed. Based on the fundamental theory of Li-Fi technology, this dual-gate phototransistor can be used as a photodetector to receive signal and encrypt electrically, magnetically, and optically for secured communication and authentication.
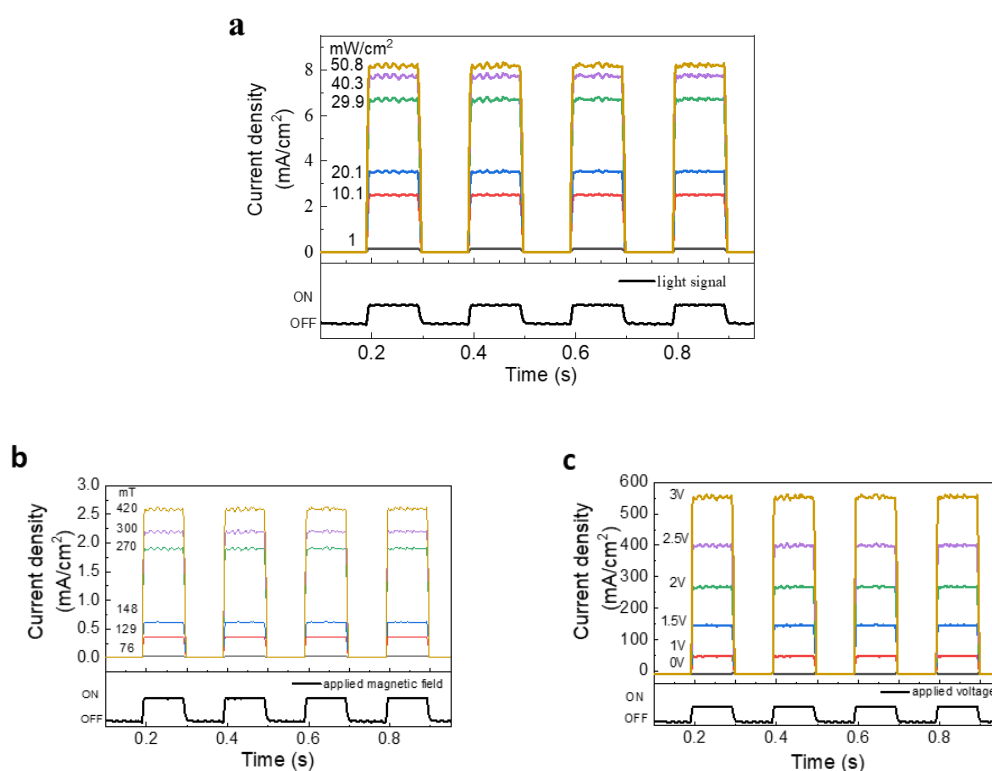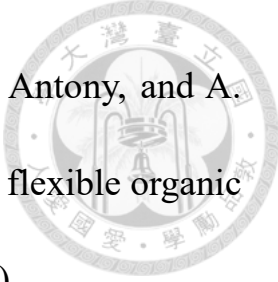

Figure 4.10 In the ON state of RRAM, the output signal of the phototransistor under **(a)** different light intensity at B = 330 mT, **(b)** different magnetic fields at I = 10.76 mW/cm^2, and **(c)** different operation voltage at one sun and B = 330 mT.

Reference

1. K. H. Kim, S. Y. Bae, Y. S. Kim, J. A. Hur, M. H. Hoang, T. W. Lee, M. J. Cho, Y. Kim, M. Kim, and J. I. Jin, Highly photosensitive J-aggregated single-crystalline organic transistors, Adv. Mater. 23, 3095-3099 (2011).

2. T. P. I. Saragi, R. Pudzich, T. Fuhrmann, and J. Salbeck, Organic phototransistor based on intramolecular charge transfer in a bifunctional spiro compound, Appl. Phys. Lett. 84, 2334-2336 (2004).

3. M. Y. Cho, S. J. Kim, Y. D. Han, D. H. Park, K. H. Kim, D. H. Choi, and J. Joo, Highly sensitive, photocontrolled, organic thin-film transistors using soluble star-shaped conjugated molecules, Adv. Funct. Mater. 18, 2905-2912 (2008).

4. J. Labram, P. Wöbkenberg, D. Bradley, and T. Anthopoulos, Low-voltage ambipolar phototransistors based on a pentacene/PC61BM heterostructure and a self-assembled nano-dielectric, Org. Electron. 11, 1250-1254 (2010).

5. S. M. Mok, F. Yan, and H. L. Chan, Organic phototransistor based on poly(3-hexylthiophene)/TiO2 nanoparticle composite, Appl. Phys. Lett. 93, 023310 (2008).

6. B. Lucas, A. El Amrani, M. Chakaroun, B. Ratier, R. Antony, and A. Moliton, Ultraviolet light effect on electrical properties of a flexible organic thin film transistor, Thin Solid Films 517, 6280-6282 (2009).

7. S. Dutta and K. Narayan, Photoinduced charge transport in polymer field effect transistors, Synthetic Met. 146, 321-324 (2004).

8. B. Mukherjee, M. Mukherjee, Y. Choi, and S. Pyo, Organic Phototransistor with n-Type Semiconductor Channel and Polymeric Gate Dielectric, J. Phys. Chem. C 113, 18870-18873 (2009).

9. T. D. Anthopoulos, Electro-optical circuits based on light-sensing ambipolar organic field-effect transistors, Appl. Phys. Lett. 91, 113513 (2007).

Chapter 5 Conclusion

We have demonstrated a novel dual-gate phototransistor by stacking magnetoelectronic device, RRAM and OSC in tandem. By applying light, voltage and magnetic field, one can control the output current of the phototransistor with high ON/OFF ratio of 10^3. The photoresponse time of the dual-gate phototransistor is 3 μs, which is ultra-fast compared to typical field-effect phototransistor. This triple control, electric, photonic, and magnetic dual-gate phototransistor with ultra-fast photoresponse time offers diverse applications in information transmission for communication. We believe that our designed device is very useful and timely, which can play an important role for the development of future information technology.